Low Level Jet Streams at the Sea Ice Edge - Numerical Simulations using WRF

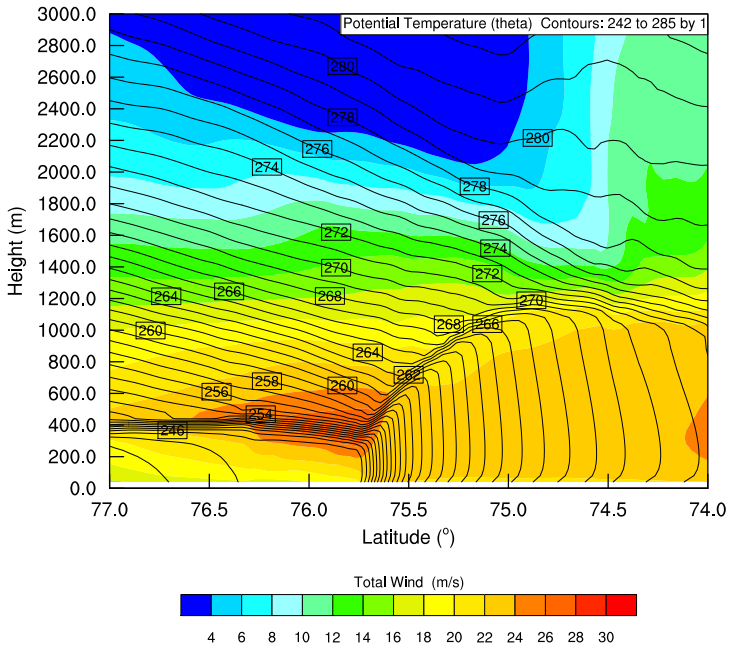

Master's Thesis in Meteorology

Stefan Keiderling

June 3, 2013

UNIVERSITY OF BERGEN
GEOPHYSICAL INSTITUTE

The front page figure shows a south-north cross section extending from 74°N to 77°N at 26°E. The colored shading depicts the total wind speed and the contours illustrate the potential temperature. The sea ice edge can be found just to the north of the strong surface potential temperature gradient at 75.7°N. A low level wind maximum is evident in the vicinity of the sea ice edge at around 400 m altitude.

Abstract

The goal of the presented thesis is to investigate the formation of low level jets at the sea ice edge. Differential heating creates very sharp fronts at the ice edge. A transversal circulation, initiated by altered pressure gradients, influences the speed of the geostrophic wind and therefore can create low level jets.

The Weather Research and Forecast Model (WRF) was used to simulate three different cases. An analysis of the geostrophic wind suggested that the ice edge jet simulated by GRØNÅS and SKEIE (1999) is not forced by the ice edge but rather by a slowing down of the proximate flow. Similar results were obtained in a simulation of measurements by DRÜE and HEINEMANN (2001). The atmospheric situation in both cases was comparable. The large scale flow had the sea ice edge to the right and the thermal wind was directed in the opposite direction. However, the measurements did not contain a low level jet. Furthermore, a discrepancy regarding frictional processes over sea ice was revealed. The only measured ice edge jet by SHAPIRO and FEDOR (1989) could not be reproduced. This case, however, showed a complex setting of the atmosphere and it was not clear if the forcing of the low level jet was only due to the ice edge. Future work will focus on idealized cases in order to increase the quality of ice edge jet predictions.

Acknowledgment

I am very grateful to my supervisor Thomas Spengler who guided me to the very fascinating field of atmospheric dynamics at the sea ice edge. I have to acknowledge his confidence in me and allowing me to work with great independence. Nevertheless, he was always available and helped me when I was struggling with the dynamics at atmospheric fronts. The collaboration has been very inspiring and I am looking forward to continuing this work. Many thanks have to be addressed to the dynamical meteorology group at the Geophysical Institute, especially to Annick Terpstra who fixed a lot of my WRF issues.

I really have to thank my Svalbardian fellow students who convinced me that joining them to Bergen would be a great idea. They were right. However, all students at Høytrykket and Odd and the people at the Geophysical Institute made my master studies a very great time.

Although not being physically present most of the time, I am deeply grateful to my family and friends back home who supported me throughout 6 years of studying and never doubted that I can make it. I could not have done this without you.

Contents

Chapter 1

Introduction

Marine activities at high latitudes are often encountering difficult conditions. Especially rough seas caused by strong winds can lead to dangerous situations. Not only the ocean is affected by the wind also the sea ice is influenced by the wind. It can get packed, so that vessels staying in the marginal ice zone (MIZ) get caught and are not able to leave the MIZ safely. In order to avoid severe accidents it is necessary to give precise warnings to ships operating in the Arctic Seas. There are still a lot of processes in the Arctic atmosphere which are not well understood. This makes it challenging to predict potential hazardous events. A better understanding of the atmosphere in the Arctic can improve the performance of numerical weather predictions and thus yield to better warnings.

One phenomenon which causes severe conditions and which still needs more research are low level jets. Low level jets can be induced by many different processes. This thesis will focus on such jet streams created at the sea ice edge. The edge between the open ocean and the sea ice marks a very distinct border in terms of surface heat flux. The sensible heat flux over sea ice is small, e.g. VIHMA *et al.* (2009) measured -4 to $-6\mathrm{W/m^2}$. On the other hand, sensible heat fluxes over open ocean can for example reach values up to $300\mathrm{W/m^2}$ (PETERSEN and RENFREW (2009)).

There has been some studies regarding this topic in the late 1980's and 1990's. SHAPIRO

and FEDOR (1989) and LANGLAND *et al.* (1989) report about a low level jet event on 14 February 1984. This case is based on aircraft measurements during the Arctic Cyclone Experiment (ACE). An ice edge jet on 12 January 1993 was part of the work by GRØNÅS and SKEIE (1999) and ØKLAND (1998). Both cases have in common that the wind is parallel or close to parallel along the ice edge. LANGLAND *et al.* (1989) GLENDENING (1994) make additional experiments about the sensitivity of the wind speed maximum to the relative direction of the wind. The above mentioned papers emphasize the strong connection between the low level jet and a strong front at the ice edge. Furthermore, SHAPIRO and FEDOR (1989) suggest that "The physical structure of this boundary-layer jet-front system [...] is analogous to that of the upper tropospheric jet-front tropopause folds" (p. 266). A similar explanation is given by LANGLAND *et al.* (1989), they state that the intensification of the wind is mainly due to thermal wind mechanisms. They also suggest that the transversal circulation at the front increases the along-front wind by coriolis turning of the ageostrophic wind.

The cases in 1984 and 1993 differ in terms of geographical alignment and relative position of the ice edge. Whereas the 1984 case is south-north aligned and with the ice edge to the left of the flow, the case from 1993 is east-west aligned and has the ice edge to the right of the flow. The latter is the result of simulations and originates from experiences made by a Norwegian coast guard ship which observed hurricane force winds. GRØNÅS and SKEIE (1999) tried to simulate this case but with an emphasis on an Arctic front in the Barents Sea. The ice edge jet is just a minor point and is explained by a general wind increase due to an approaching occlusion front. They state furthermore that strong temperature and pressure gradients would lead to a geostrophic wind of 70 m/s. A mathematical approach is given by ØKLAND (1998) who also refers to the observations of the coast guard vessel. This paper solves the equations given by ELIASSEN (1951) with a point source of sensible heat. The results show an increase of the along ice edge wind speed by 10 m/s due to the differential surface heat flux.

Aircraft based measurements of flow along the ice edge west of Greenland were taken by DRÜE and HEINEMANN (2001) during a measuring campaign in April 1997. In

contrast to SHAPIRO and FEDOR (1989), this case in 1997 did not show an ice edge jet. As in the 1993 case, the flow in DRÜE and HEINEMANN (2001) has the sea ice to the right, which differs to the observations made by SHAPIRO and FEDOR (1989) where the sea ice is to the left of the flow.

This thesis will consider the 1984, 1993 and 1997 case. The Weather Research and Forecasting (WRF) model was used to simulate all three cases. The model was initialized with ERA-Interim data from the European Centre for Medium-Range Weather Forecasts (ECMWF). The first step will be to simulate the results from SHAPIRO and FEDOR (1989), GRØNÅS and SKEIE (1999) and DRÜE and HEINEMANN (2001). Afterwards there will be a geostrophic analysis of each case, respectively.

Chapter two will give an overview about the theory of semi-geostrophic frontogenesis, transversal circulation, thermal wind relation and tropopause folding. A description of the WRF model and the post processing will be given in chapter 3. Chapter 4 describes the results from the 1984 case. The simulation and analysis of the 1993 case is presented in chapter 5. The 1997 case is the subject in chapter 6, where the outcome of the simulation is shown and analyzed. Finally, there will be a summary of this thesis and an outlook in chapter 7.

Chapter 2

Theory

This chapter gives an introduction to the theory which is used for the purpose of explaining the processes occurring at boundary layer fronts. The term boundary layer fronts refers to sharp gradients within the boundary layer caused by surface characteristics. First, there will be an overview about semi-geostrophy which is appropriate for flows in frontal regions. Second, a section about front development follows. The third part is a summary about the formation of jets at fronts. Finally, an overview about the thermal wind relation and tropopause folding is given. The variables used in the following sections are summarized in Table 2.1.

2.1 Semi-geostrophy

Semi-geostrophy is applied when the momentum can be approximated by its geostrophic value. This is the case in frontal regions, where there is a difference in the order of magnitude in along and across frontal length scales and velocities. For example the sea ice edge in the Barents Sea is such an area where fronts develop which are about 1000 km in the east-west direction and about 100 km in the south-north direction. Also, the velocities along the front are in general much higher than across front velocities. This difference in scales leads to a different importance of the inertial and coriolis terms in the horizontal momentum equation. The ratio of both terms are known as the Rossby

Symbol	Physical Quantity
x,y,z	Coordinates of a Cartesian coordinate system
t	Time
u	Wind speed in x-direction
v	Wind speed in y-direction
w	Wind speed in z-direction
p	Atmospheric pressure, also used as vertical coordinate
ω	Vertical wind speed in p-direction
T	Temperature
ρ	Density
α	Inverse Density
R	Gas constant of dry air
c_p	Heat capacity at constant pressure
g	Gravitational acceleration
ϕ	Geopotential
Θ	Potential Temperature
f	Coriolis Parameter
u_g	Geostrophic wind in x-direction
v_g	Geostrophic wind in y-direction
v_a	Ageostrophic wind in y-direction
$\boldsymbol{\zeta}^a$	Three-dimensional absolute vorticity vector
ψ	Three-dimensional stream function

Table 2.1: Overview of used variables

number. The horizontal momentum equations in z-coordinates are as follows.

$$\frac{Du}{Dt} - fv + \frac{\partial p}{\partial x} = 0 \tag{2.1}$$

$$\frac{Dv}{Dt} + fu + \frac{\partial p}{\partial y} = 0 \tag{2.2}$$

Friction is neglected. Here, D is the total derivative and ∂ is the partial derivative. The coordinate system is aligned with the front. So, the x-coordinate is along the front and the y-coordinate is aligned across the front. Here u and v are the along and across front velocities, respectively. With the length and velocity scales $L_x = 1000\text{km}, L_y = 100\,\text{km}, U = 10\,\text{m/s}$ and $V = 1\,\text{m/s}$ and using the definition of the Rossby number HOLTON (2004), follows

$$RO = \frac{|Du/Dt|}{|fv|} \sim \frac{UV/L_y}{fV} \sim \frac{10\text{m/s}}{100\text{km}\,10^{-4}\text{s}^{-1}} \sim 1 \tag{2.3}$$

$$RO = \frac{|Dv/Dt|}{|fu|} \sim \frac{V^2/L_y}{fU} \sim \frac{(1\text{m/s})^2}{10\text{m/s}\,1000\text{km}\,10^{-4}\text{s}^{-1}} \sim 10^{-2} \tag{2.4}$$

(2.4) shows that the along front velocity u is in geostrophic balance. A Rossby number of 10^{-2} indicates that the coriolis term in (2.2) is two orders of magnitude larger than the inertial term. So the pressure gradient term in (2.2) is the only who can balance the coriolis term, which is the definition of geostrophy. On the other hand, v is not in geostrophic balance, since the inertia is of equal magnitude as the coriolis effect. With that finding the velocities can be split up in a geostrophic and ageostrophic part. The scale analysis showed that u is purely geostrophic and so we approximate u with u_g, the geostrophic wind.

$$u_g = -\frac{1}{f\rho}\frac{\partial p}{\partial y} \tag{2.5}$$

v is not in geostrophic balance, hence a ageostrophic part is added $v = v_g + v_a$. Now the horizontal momentum equation (2.1) can be rewritten.

$$\begin{aligned} \frac{Du_g}{Dt} - fv_g - fv_a + \frac{1}{\rho}\frac{\partial p}{\partial x} &= 0 \\ \frac{Du_g}{Dt} - fv_a &= 0 \end{aligned} \tag{2.6}$$

Where the definition of the geostrophic wind in v-direction was used.

$$fv_g = \frac{1}{\rho}\frac{\partial p}{\partial x} \tag{2.7}$$

The momentum in along front direction is approximated with the geostrophic momentum and therefore it is known as geostrophic momentum approximation HOSKINS (1975). It is applied in order to analyze fronts and the geostrophic wind connected to them. (2.6) states that the geostrophic wind along a front can only be changed by ageostrophic wind across the front.

2.2 Semi-geostrophic frontogenesis

In order to explain the development of ice edge jets it is necessary to understand the mechanisms of semi-geostrophic frontogenesis and transversal circulations at atmospheric fronts. Pioneer work on this field has been done throughout the 20th century by the great Norwegian meteorologists Vilhelm Bjerknes, Jacob Bjerknes, Arnt Eliassen, Hans Økland and Sigbjørn Grønås as well as the British meteorologists Sir Brian Hoskins and John Sawyer. Their theories are applicable to frontal zones in general, but with a main focus on frontogenesis caused by horizontal deformation fields. In the case of ice edge jets the frontal zone is set up by differential heating. The relative cold airmass over the ice and the large surface heat fluxes over the open water are the main forcing for frontogenesis in this case. So first, there will be an analysis of the genesis of the front at the sea ice edge. Afterwards the focus will be on the associated transversal circulation and finally the formation of low level jet streams will be explained.

The most famous work on the development of fronts in the atmosphere has been done by the Bergen School of Meteorology in the 1920's (BJERKNES J. (1919); BJERKNES V. (1921); BJERKNES J. and SOLBERG H. (1922)). They introduced the concept of the polar front, which states that cold air masses from the north and warm air masses from the south build a very distinct border. These fronts are regarded as a cause

for cyclones. An analytical description of how fronts can develop was first given by PETTERSSEN (1936); MILLER (1948), equation (2.8).

$$\begin{aligned} F = & \frac{1}{|\nabla\theta|}\frac{\partial\theta}{\partial x}\left(\frac{\partial\dot{Q}}{\partial x} - \frac{\partial u}{\partial x}\frac{\partial\theta}{\partial x} - \frac{\partial v}{\partial x}\frac{\partial\theta}{\partial y} - \frac{\partial w}{\partial x}\frac{\partial\theta}{\partial z}\right) \\ & + \frac{1}{|\nabla\theta|}\frac{\partial\theta}{\partial y}\left(\frac{\partial\dot{Q}}{\partial y} - \frac{\partial u}{\partial y}\frac{\partial\theta}{\partial x} - \frac{\partial v}{\partial y}\frac{\partial\theta}{\partial y} - \frac{\partial w}{\partial y}\frac{\partial\theta}{\partial z}\right) \\ & + \frac{1}{|\nabla\theta|}\frac{\partial\theta}{\partial z}\left(\frac{\partial\dot{Q}}{\partial z} - \frac{\partial u}{\partial z}\frac{\partial\theta}{\partial x} - \frac{\partial v}{\partial z}\frac{\partial\theta}{\partial y} - \frac{\partial w}{\partial z}\frac{\partial\theta}{\partial z}\right) \end{aligned} \tag{2.8}$$

∇ is the Del-operator. They state that horizontal gradients can be sharpened by shearing or stretching deformation, tilting or differential heating. This is known as the kinematic approach. It does not take advection nor local changes into account. In contrast, those are included in the geostrophic momentum approximation (HOSKINS (1975)) which is the basis for the semi-geostrophic frontogenesis theory. This theory contains advection of geostrophic momentum and heat by ageostrophic flow. The ageostrophic flow at atmospheric fronts can be explained as followed. The geostrophic wind tries to drive the frontal system away from thermal wind balance by increasing the horizontal temperature gradient. In order to maintain this balance an ageostrophic circulation starts. This circulation acts in two ways. First, on the cold side sinking motion leads to adiabatic warming. Rising air on the warm side leads to adiabatic cooling. Thus, the horizontal temperature gradient is decreased. Second, if the ageostrophic wind at the surface is directed in the opposite direction to the upper branch of the circulation, the geostrophic wind will be accelerated in opposing directions. The result is an increased vertical shear and in combination with the first mechanism, thermal wind balance is achieved (see section 2.4).

Semi-geostrophy allows much faster and stronger front development, since gradients in temperature or momentum can be sharpened more effectively by ageostrophic flow. Also the typical tilt of fronts can be explained by semi-geostrophy. The frontogenetic process is depicted by the Sawyer-Eliassen equation (2.9) ELIASSEN (1962); SAWYER

(1956) as described in BLUESTEIN (1993).

$$a\frac{\partial^2\psi}{\partial y^2} + b\frac{\partial^2\psi}{\partial y \partial p} + c\frac{\partial^2\psi}{\partial p^2} = 2\frac{R}{f_0 p}\left(\frac{p}{p_0}\right)^{\kappa}\left(\frac{\partial\theta}{\partial y}\frac{\partial v_g}{y} + \frac{\partial\theta}{\partial x}\frac{\partial u_g}{\partial y}\right) - \frac{R}{c_p f_0 p}\frac{\partial}{\partial y}\left(\frac{dQ}{dt}\right) \quad (2.9)$$

where

$$a = -\frac{R}{f_0 p}\left(\frac{p}{p_0}\right)^{\kappa}\frac{\partial\theta}{\partial p}, \quad b = 2\frac{\partial u_g}{\partial p} = 2\frac{R}{f_0 p}\left(\frac{p}{p_0}\right)^{\kappa}\frac{\partial\theta}{\partial y}, \quad c = f_0 - \frac{\partial u_g}{\partial y}$$

Where κ is defined as R/c_p. The coefficients a, b and c are static,baroclinic and inertial stability, respectively. With equation (2.9), it is possible to calculate the ageostrophic circulation if the forcing terms on the right hand side of (2.9) and the stability coefficients a, b and c are known. A simple example is given in LIN (2010) (p.392-394). There, the frontogenetic forcing is given by a confluent flow which means that geostrophic wind is advecting cold air from the north and warm air from the south, thus, a front develops (Figure 2.1). No diabatic heating is included, this means the second term on the right hand side of (2.9) is zero. Furthermore, it is assumed that there are no potential temperature changes along the x-axis, which yields $\partial\theta/\partial x = 0$. This kind of setup is also known as Bergeron forcing, named after Tor Bergeron (1891-1971) a Swedish meteorologists and member of the Bergen School of Meteorology. Analyzing the temperature and wind field yields $\partial v_g/\partial y < 0$ and $\partial\theta/\partial y < 0$, so the forcing term becomes also positive. The coefficient (a) is greater than 0 when assuming a statically stable atmosphere ($\partial\theta/\partial p < 0$). The inertial stability coefficient (c) is also positive when neglecting a shear of u_g in y-direction. Consequential are $\partial^2\psi/\partial y^2 > 0$ and $\partial^2\psi/\partial p^2 > 0$ (the second term on the left hand side of (2.9) is neglected, an explanation is given below). Here, ψ is the streamfunction and it describes the flow of a fluid. Velocities can directly be derived from ψ. The following definition is used,

$$v_a = -\frac{\partial\psi}{\partial p} \quad (2.10)$$

$$\omega = \frac{\partial\psi}{\partial y} \quad (2.11)$$

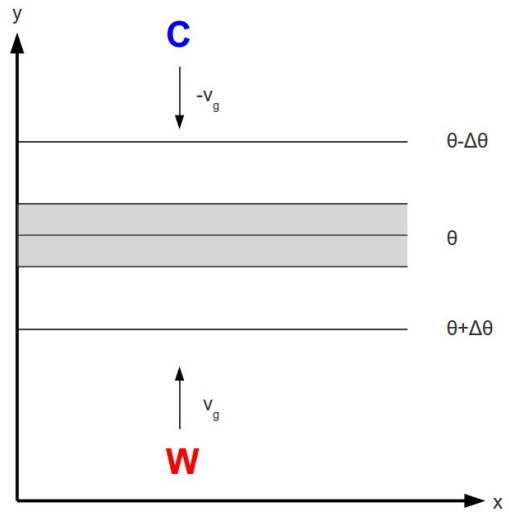

Figure 2.1: Frontogenesis by stretching deformation (Bergeron Forcing)

With (2.10) and (2.11) the ageostrophic circulation at a front can be described qualitatively, since

$$\frac{\partial^2 \psi}{\partial p^2} = -\frac{\partial v_a}{\partial p} > 0 \Rightarrow \frac{\partial v_a}{\partial p} < 0 \tag{2.12}$$

$$\frac{\partial^2 \psi}{\partial y^2} = \frac{\partial \omega}{\partial y} > 0 \tag{2.13}$$

Thus v_a is increasing with height and ω is increasing northward, yielding a clockwise circulation (see Figure 2.2). Figure 2.2 depicts a fairly simple model of an ageostrophic circulation. For example there is no tilt of the frontal zone visible. The reason is the disregard of the second term on the left hand side of (2.9) which means that there is no change of ω in p-direction and no change of v_a in y-direction.

$$\frac{\partial^2 \psi}{\partial y \partial p} = \frac{\partial \omega}{\partial p} = -\frac{\partial v_a}{\partial y} = 0 \tag{2.14}$$

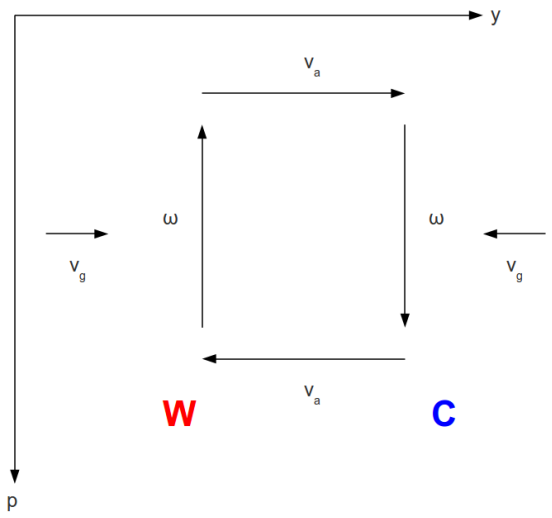

Figure 2.2: Ageostrophic circulation induced by a Bergeron forcing)

2.3 Jet-formation at fronts

The previous section showed that the ageostrophic circulation is set up in order to maintain thermal-wind balance. By using the geostrophic momentum approximation by HOSKINS (1975), the ageostrophic wind component translates into an increase of the geostrophic wind with time.

$$\frac{Du_g}{Dt} = fv_a \tag{2.15}$$

The idea of an increase of geostrophic wind by an ageostrophic circulation was presented in a paper by NAMIAS and CLAPP (1949) and was named confluence theory. The theory tries to give an explanation for the high tropospheric jet stream at the polar front. In NAMIAS and CLAPP (1949) an idealized case is considered in which frontogenesis happens due to a deformation field suggested by Bergeron. Therefore, the theory is called confluence theory. Cold air from the north and warm air from the south are confluent and than turn to the east (See Figure 2.3). This kind of flow

pattern leads to an increased meridional temperature gradient. As the warm and cold airmass converge, the pressure gradient increases. The initial easterly flow is then sub-geostrophic and needs to be adapted to the new pressure field, which is done by the ageostrophic circulation. At the surface is the pressure gradient directed from north to south. Warmer air has a larger extension than colder air, therefore, the warm column in the south is stretched vertically which leads to higher potential energy. This will initiate a mass flow in order to balance the different potential energies. Hence, the column with colder air gains mass which in turn lead to higher pressure at the surface. As the deformation forcing acts on this air masses and further increases the temperature gradient, consequently the pressure gradient force also increases and is not in balance with the Coriolis force anymore. This imbalance is resulting in ageostrophic accelerations. This additional acceleration leads to an increase in the Coriolis force, which again balances the pressure gradient force. Since both forces are intensified, the geostrophic wind will also be increased and a jet forms. This theory originally was developed for the high tropospheric polar front jet which is of planetary scale. However, this explanation is valid for all flows with a small Rossby number. Thus, the jet formation, like explained in the confluence theory by NAMIAS and CLAPP (1949), is probably also applicable for wind maxima at the sea ice edge.

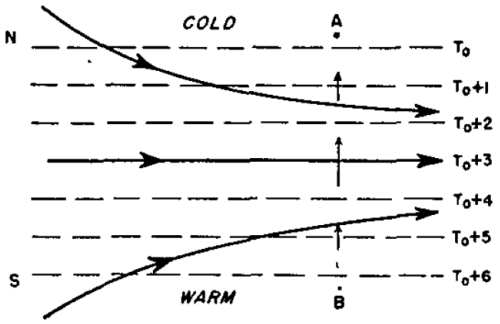

Figure 2.3: Confluent flow with warm air from the south and cold air from the north. From Figure 3 in NAMIAS and CLAPP (1949)

2.4 Thermal Wind Relation

The geostrophic wind not only changes in time by an ageostrophic circulation but it also changes with height. The prerequisite for an increasing or decreasing geostrophic wind with height is a horizontal temperature gradient which clearly exists at the ice edge. The temperature is directly proportional to the thickness of a layer between two pressure surfaces. This follows from the hydrostatic approximation (2.16).

$$\frac{\partial p}{\partial z} = -\rho g \tag{2.16}$$

Using the ideal gas law

$$\rho = \frac{p}{RT} \tag{2.17}$$

,it follows

$$\partial z = \frac{RT}{g} \partial \ln p \tag{2.18}$$

In pressure coordinates, the geopotential ϕ is introduced. The definition of its differential is $\partial\phi = g\partial z$. It corresponds to the work which is needed to lift an unit mass about ∂z. So (2.18) can be written as

$$\partial\phi = RT\partial \ln p \tag{2.19}$$

Thus, the geopotential difference between to pressure surfaces is proportional to the temperature. We will show that differences in geopotential cause a geostrophic wind. First we transform the geostrophic wind from z-coordinates to p-coordinates by using the hydrostatic approximation in p-coordinates $\partial p = -g\partial\phi$. The following derivations are only with regard to the geostrophic wind in x-direction.

$$u_g = -\frac{1}{f}\frac{\partial \phi}{\partial y} \tag{2.20}$$

The change of the geostrophic wind with height is obtained by differentiating (2.20) with respect to p.

$$\frac{\partial u_g}{\partial p} = -\frac{1}{f}\frac{\partial}{\partial y}\frac{\partial \phi}{\partial p} \tag{2.21}$$

Again using the hydrostatic approximation and the ideal gas law $\alpha = \frac{RT}{p}$ with α being the inverse density, it follows

$$\begin{aligned} \frac{\partial u_g}{\partial p} &= \frac{1}{f}\frac{\partial \alpha}{\partial y} \\ &= \frac{R}{fp}\frac{\partial T}{\partial y} \\ \frac{\partial u_g}{\partial \ln p} &= \frac{R}{f}\frac{\partial T}{\partial y} \end{aligned} \tag{2.22}$$

$\partial p/\partial y$ is zero, since the pressure is constant on isobaric surfaces. (2.22) shows that a negative meridional temperature gradient causes an increase of the geostrophic wind with height towards east. The difference between the geostrophic winds at two different heights is called thermal wind. Figure 2.4 illustrates the relation between the temperature, the geopotential and the geostrophic wind.

We also need the thermal wind in z-coordinates, since later we will have scalar fields interpolated to a z-coordinate system (see chapter 3). Therefore we take the z-derivative of (2.5).

$$\frac{\partial u_g}{\partial z} = -\frac{1}{\rho f}\frac{\partial^2 p}{\partial y \partial z} + \frac{1}{\rho^2 f}\frac{\partial \rho}{\partial z}\frac{\partial p}{\partial y} \tag{2.23}$$

Combining with (2.16), yields

$$\begin{aligned} \frac{\partial u_g}{\partial z} &= \frac{g}{f}\frac{\partial \ln \rho}{\partial y} + \frac{1}{\rho^2 f}\frac{\partial \rho}{\partial z}\frac{\partial p}{\partial y} \\ &= \frac{g}{f}\frac{\partial \ln \rho}{\partial y} + \frac{1}{\rho^2 f}\frac{\partial p}{\partial y}\frac{\partial p}{\partial z}\frac{1}{RT} + \frac{1}{\rho^2 f}\frac{\partial p}{\partial y}\left(-\frac{1}{T^2}\right)\frac{\partial T}{\partial z}\frac{p}{R} \\ &= \frac{g}{f}\frac{\partial \ln \rho}{\partial y} - \frac{g}{f}\frac{\partial \ln p}{\partial y} - \frac{1}{\rho f}\frac{\partial p}{\partial y}\frac{\partial \ln T}{\partial z} \end{aligned} \tag{2.24}$$

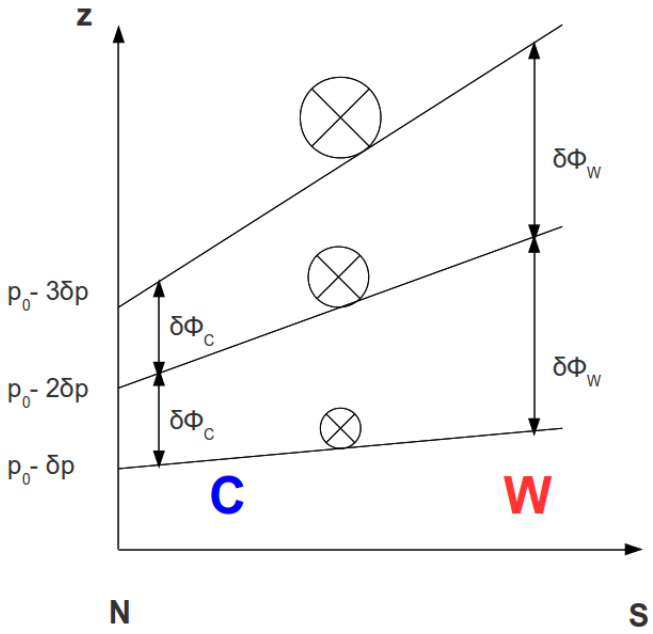

Figure 2.4: Schematic showing the change of the geostrophic wind with height due to a horizontal temperature gradient.

Again, the ideal gas law and the hydrostatic approximation was used. The following relation can also be obtained from (2.17).

$$\begin{aligned} \partial p &= \partial \rho RT + \partial T \rho R \\ \partial \ln p &= \frac{RT}{p}\partial \rho + \partial T \frac{\rho R}{p} \\ \partial \ln p &= \partial \ln \rho + \partial \ln T \end{aligned} \tag{2.25}$$

Then (2.24) can be written as

$$\frac{\partial u_g}{\partial z} = -\frac{g}{f}\frac{\partial \ln T}{\partial y} + u_g \frac{\partial \ln T}{\partial z} \tag{2.26}$$

(2.26) is the change of the geostrophic wind with height in dependency of the tem-

perature. For further studies it is more convenient to have the thermal wind relation in dependency of the potential temperature (see chapter 3). The definition of the potential temperature is

$$\Theta = T\left(\frac{p_0}{p}\right)^{\frac{R}{c_p}} \tag{2.27}$$

With (2.27), $\frac{\partial \ln T}{\partial y}$ can be written as

$$\begin{aligned}\frac{\partial \ln T}{\partial y} &= \frac{1}{T}\left[\left(\frac{p_0}{p}\right)^{\frac{-R}{c_p}}\frac{\partial \Theta}{\partial y} + \Theta\left(\frac{-R}{c_p}\right)\left(\frac{p_0}{p}\right)^{\frac{-R}{c_p}}\left(\frac{p_0}{p}\right)^{-1}\left(\frac{-p_0}{p^2}\right)\frac{\partial p}{\partial y}\right] \\ &= \frac{\partial \ln \Theta}{\partial y} + \frac{\Theta}{T}\left(\frac{p_0}{p}\right)^{\frac{-R}{c_p}}\left(\frac{R}{c_p}\right)\frac{p}{p_0}\frac{p_0}{p^2}\frac{\partial p}{\partial y} \\ &= \frac{\partial \ln \Theta}{\partial y} + \frac{R}{c_p}\frac{\partial \ln p}{\partial y}\end{aligned} \tag{2.28}$$

We apply (2.28) also for $\frac{\partial \ln T}{\partial z}$. The thermal wind relation in z-coordinates and in dependency of the potential temperature reads then as

$$\begin{aligned}\frac{\partial u_g}{\partial z} &= -\frac{g}{f}\frac{\partial \ln \Theta}{\partial y} - \frac{R}{c_p}\frac{g}{f}\frac{\partial \ln p}{\partial y} + u_g\left[\frac{\partial \ln \Theta}{\partial z} + \frac{R}{c_p}\frac{\partial \ln p}{\partial z}\right] \\ &= -\frac{g}{f}\frac{\partial \ln \Theta}{\partial y} + u_g\frac{\partial \ln \Theta}{\partial z} - \frac{R}{c_p}\frac{g}{fp}\frac{\partial p}{\partial y} + \frac{u_g}{p}\frac{R}{c_p}\frac{\partial p}{\partial z} \\ &= -\frac{g}{f}\frac{\partial \ln \Theta}{\partial y} + u_g\frac{\partial \ln \Theta}{\partial z} - \frac{R}{c_p}\frac{g}{fp}\frac{\partial p}{\partial y} + \left(\frac{1}{\rho f}\frac{\partial p}{\partial y}\right)\frac{R}{c_p p}(\rho g) \\ &= -\frac{g}{f}\frac{\partial \ln \Theta}{\partial y} + u_g\frac{\partial \ln \Theta}{\partial z}\end{aligned} \tag{2.29}$$

The equation above looks similar to (2.26). It describes the change of the geostrophic wind with height due to gradients in potential temperature. The first term on the right hand side of (2.29) states that whenever there is a negative meridional gradient in potential temperature the geostrophic wind will increase with height toward the east. This fact was already clear from (2.22), but in z-coordinates there is an additional term. The second term on the right hand side states that a eastward geostrophic wind will increase with height toward the east and a westward geostrophic wind will increase with height toward the west if the atmosphere is stably stratified ($\partial \ln \Theta / \partial z > 0$). A scale

analysis will show the relative importance of both terms. For this purpose we rearrange (2.29).

$$\frac{\partial u_g}{\partial z} = \frac{g}{f}\left(\frac{u_g f}{g}\frac{\partial \ln\Theta}{\partial z} - \frac{\partial \ln\Theta}{\partial y}\right) \tag{2.30}$$

We assume following typical values $u_g \approx 10\text{m/s}$, $f \approx 10^{-4}$ and $g \approx 10$. So we obtain

$$\frac{u_g f}{g} = \frac{10 * 10^{-4}}{10} = 10^{-4} \tag{2.31}$$

Thus, the absolute value of $\frac{\partial \ln\Theta}{\partial z}$ is decreased by 10^{-4}. Therefore, the thermal wind is mainly determined by the meridional change of $\ln\Theta$.

2.5 Tropopause Folding

The intrusion of stratospheric air into the troposphere is called tropopause folding. Stratospheric air masses are characterized by high potential vorticity (PV). The Ertel's potential vorticity is defined by

$$PV = \frac{\boldsymbol{\zeta}^a \cdot \nabla\theta}{\rho} \tag{2.32}$$

Here, $\nabla\theta$ is the three-dimensional potential temperature gradient.Hence, in case of a tropopause folding, isolines of high potential vorticity are dipping deep down into the troposphere (see HOLTON (2004), p.145 and WALLACE and HOBBS (2006), p.334). As (2.32) shows, high PV is associated with high gradients in potential temperature. The tropopause is a region with strong static stability, this means that the potential temperature increases very fast with height. When the tropopause folds down, the strong vertical potential temperature gradient gets tilted and forms a frontal zone with strong horizontal potential temperature gradients. A horizontal temperature gradient is causing an increase of the geostrophic wind with height (see section 5.5.3). This frontal zone can persist throughout the whole troposphere and therefore there is a constant increase of the geostrophic wind with height, which leads to the upper level jet stream.

Chapter 3

Method

In order to gain understanding of the processes at the sea ice edge, we simulated the atmosphere with the aid of a numerical model. We chose the Weather Research and Forecasting (WRF) model for reproducing the results of SHAPIRO and FEDOR (1989); GRØNÅS and SKEIE (1999) and DRÜE and HEINEMANN (2001). This model is a collaboration work by the National Center for Atmospheric Research (NCAR), the National Center for Environmental Prediction (NCEP), the Earth System Research Laboratory (ESRL), the Department of Defense's Air Force Weather Agency(AFWA), the Naval Research Laboratory (NRL), the Center for Analysis and Prediction of Storms (CAPS) and the Federal Aviation Administration (FAA).

3.1 Model Structure

WRF can simulate idealized and real cases. The data for the initialization is provided by the reanalysis product ERA-Interim from the European Centre for Medium-Range Weather Forecast (ECMWF). ERA-Interim covers a period from 1979 until present. In order to initialize WRF a preprocessing system has to be applied. The WRF Preprocessing System (WPS) consists of three parts. The first part is called *geogrid.exe* which defines the topography for each the domain. The geographical data for this procedure is provided by the Mesoscale and Microscale Meteorology Division of the NCAR. It is

available in 30″, 2′, 5′ and 10′ resolution. The next step is to convert the grib files from the ERA-Interim input to intermediate files. The executable for that procedure is called *ungrib.exe*. Finally, the converted input data has to be interpolated to the defined domains by *metgrid.exe*. All three WPS components are controlled by a text file called *namelist.wps*. After the preprocessing by WPS, another step is necessary before running WRF. The output from *metgrid.exe* has to be interpolated to the vertical grid and the boundary conditions have to be set. This is done by a program section called *real.exe* and was the last step before WRF can be run. The WRF executable *wrf.exe* as well as *real.exe* are also controlled by a text file. The name of this file is *namelist.input* which determines the model specifications, e.g. integration time step,time step of the model output, vertical levels, restart options, feedback options, physic and dynamic options.

3.2 Numerical Realization

There are two supported dynamical solvers, the Advanced Research WRF (ARW) and the Nonhydrostatic Mesoscale Model(NMM). The ARW solver, which we used, is developed by the Mesoscale and Microscale Meteorology Division of the NCAR. It is based on the fully compressible, nonhydrostatic Euler equations and it conserves scalar variables (see SKAMAROCK *et al.* (2008)). The vertical dimension is expressed in η-coordinates (Figure 3.1) which is terrain following and monotonically decreasing with height. The grid spacing is variable, which means that the grid in the vertical dimension is getting coarser as the height increases. The η levels are defined as a ratio between 0.0 and 1.0 (3.1). We run the model with 80 vertical levels where about 36 levels are below 3 km.

$$\eta = \frac{P_h - P_{ht}}{P_{hs} - P_{ht}} \tag{3.1}$$

Here, P_h is the hydrostatic pressure surface, P_{ht} is the pressure at the top of the model and P_{hs} is the surface pressure. The horizontal grid is a staggered Arakawa C-grid. For the time integration a 2nd- or 3rd-order Runge-Kutta scheme can be used.

The advection is realized by 2nd to 6th-order scheme. Nesting is available, with the options of one and two-way nesting.

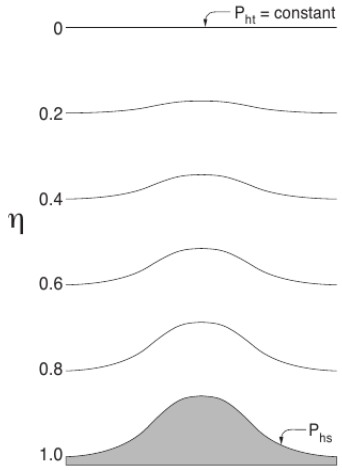

Figure 3.1: Vertical coordinate η. From SKAMAROCK *et al.* (2008)

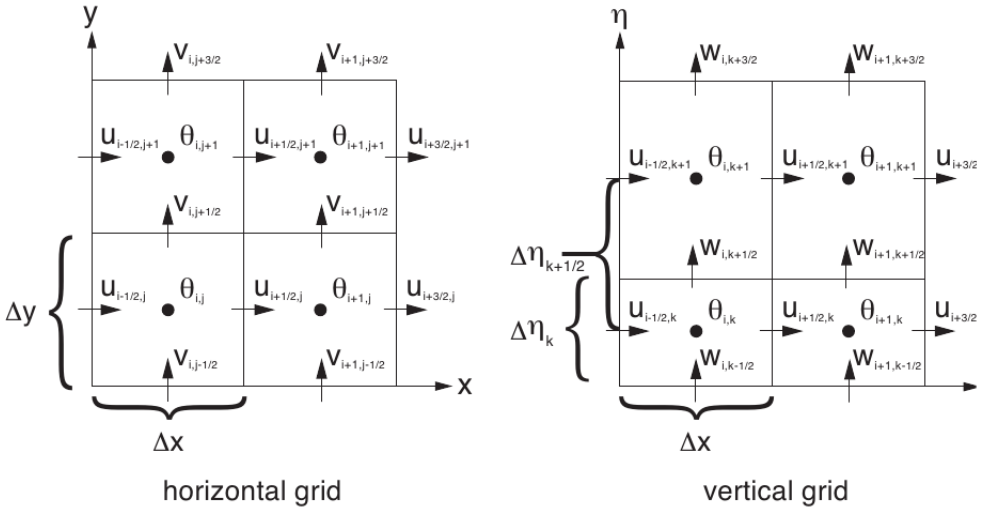

Figure 3.2: Staggered Arakawa C-grid. From SKAMAROCK *et al.* (2008)

3.3 Nesting

WRF was run for the case in 1984, 1993 and 1997. In all three cases we used three domains, with two of them being one-way nested. For the case in 1984 the setup is shown in Figure 3.3. The parent domain is covering the Greenland Sea, Svalbard and the Barents Sea and has a horizontal resolution of 9km. The second domain is one-way nested and has a resolution of 3km. It covers Svalbard and the Greenland Sea. The third domain is one-way nested in the second domain and the horizontal resolution is 1km. It includes the southern tip of Spitsbergen and the Greenland Sea in the southwest of Spitsbergen.

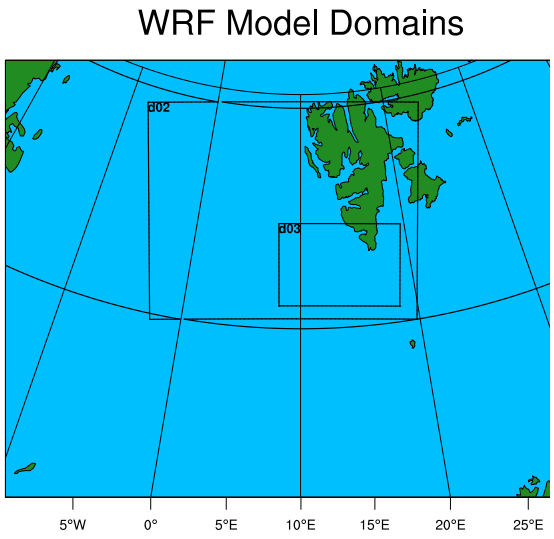

Figure 3.3: Overview of the WRF model domains for the case in 1984.

For the case in 1997, the positions of the three domains are shown in Figure 3.4. The resolutions are 27km, 9km and 3km, respectively. The parent domain covers the Davis Strait west of Greenland and extends from the Baffin Bay to the northern part of the Labrador Sea.

The setup of the domains for the 1993 case is shown in section 5.1 where a comprehensive analysis of the dependency of the model results on the horizontal resolution is presented.

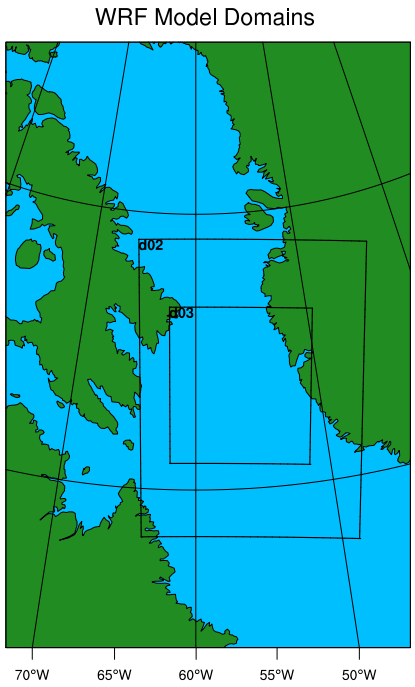

Figure 3.4: Overview of the WRF model domains for the case in 1997.

3.4 Horizontal Momentum Equations and Geostrophic Wind

Since WRF has η-coordinates in the vertical dimension, the momentum equations look a little bit different. For full description of the governing equations in the WRF model, see SKAMAROCK *et al.* (2008). Here, we neglected the curvature terms and the map factors are set to one, which implies that the grid distance always corresponds to the physical distance and that they are constant. Thus, Equation 3.2 and Equation 3.3 describe the momentum in u and v direction, respectively.

$$\frac{dU}{dt} - fV = -\frac{\mu_d}{\rho}\frac{\partial p}{\partial x} - \frac{\rho_d}{\rho}\frac{\partial p}{\partial \eta}\frac{\partial \phi}{\partial x} \tag{3.2}$$

$$\frac{dV}{dt} + fU = -\frac{\mu_d}{\rho}\frac{\partial p}{\partial y} - \frac{\rho_d}{\rho}\frac{\partial p}{\partial \eta}\frac{\partial \phi}{\partial y} \tag{3.3}$$

U and V are the velocities in x and y-direction multiplied with the dry air mass per unit area (μ_d). The dry air density is represented by ρ_d and is calculated by,

$$\rho_d = \frac{\partial \phi}{\mu_d \partial \eta} \tag{3.4}$$

The moist air density ρ is,

$$\rho = \rho_d(1 + q_{vapor} + q_{cloud} + q_{rain}) \tag{3.5}$$

Here, q_{vapor}, q_{cloud}, q_{rain} are the mixing ratios of water vapor, cloud water and rain water, respectively. As the assumption for geostrophy is a balance between the Coriolis force and the pressure gradient force, we neglect inertial accelerations ($dU/dt = 0$)and any kind of friction. Then the geostrophic wind in u direction can be expressed as,

$$u_g = \frac{1}{f\mu_d}\left[-\frac{\mu_d}{\rho}\frac{\partial p}{\partial y} - \frac{\rho_d}{\rho}\frac{\partial p}{\partial \eta}\frac{\partial \phi}{\partial y}\right] \tag{3.6}$$

The geostrophic wind in y-direction reads as,

$$v_g = \frac{1}{f\mu_d}\left[\frac{\mu_d}{\rho}\frac{\partial p}{\partial x} + \frac{\rho_d}{\rho}\frac{\partial p}{\partial \eta}\frac{\partial \phi}{\partial x}\right] \tag{3.7}$$

3.5 Parameterizations

WRF uses several parameterization for the purpose of simulating sub-grid processes which are not resolved directly. However, sub-grid processes can have an impact on the large scale flow and therefore they need to be included in the simulation. The file *namelist.input* gives in the `&physics` section an overview over the chosen parameterizations (see SKAMAROCK *et al.* (2008) for a full description of available parameterizations). The parameterization schemes used for following WRF simulations are shown in Table 3.1.

Sub-grid physics	**Parameterization Scheme**
Microphysics	WRF Single-Moment 3-class Scheme
Longwave Radiadion	Rapid Radiative Transfer Model Scheme
Shortwave Radiation	Dudhia scheme
Surface Layer	MM5 similarity
Land Surface	Unified Noah Land Surface Model
Planetary Boundary layer	Yonsei University scheme
Cumulus Parameterization	Kain-Fritsch scheme
Urban Surface	None

Table 3.1: Overview of the used WRF parameterizations

3.6 PolarWRF

In this thesis we also make use of a modified version of WRF which is especially designed for polar environments. This version is called PolarWRF and was developed by the Polar Meteorology Group of the Byrd Polar Research Center at The Ohio State University. It has several improvements. The major changes are related to the simulation of the sea ice in the Noah Land Surface Model (Noah LSM)(see SKAMAROCK *et al.* (2008) for further information about Noah LSM). PolarWRF contains a variable sea ice thickness as well as a variable snow thickness over sea ice. Furthermore, the albedo of sea ice can adapt to different seasons. As it will be shown in chapter 5, the most important modification applies to the heat transfer and the energy balance at the surface. PolarWRF includes additionally suggestions of parameterizations which are more appropriate in Arctic conditions. Table 3.2 gives an overview of the used parameterizations used for PolarWRF simulations.

Sub-grid physics	**Parameterization Scheme**
Microphysics	Morrison double-moment scheme
Longwave Radiadion	RRTMG scheme
Shortwave Radiation	RRTMG scheme
Surface Layer	Mellor-Yamada Nakanishi and Niino surface layer
Land Surface	Unified Noah Land Surface Model
Planetary Boundary layer	Mellor-Yamada Nakanishi and Niino Level 2.5 PBL
Cumulus Parameterization	Kain-Fritsch scheme
Urban Surface	None

Table 3.2: Overview of the used PolarWRF parameterizations

3.7 Numerical stability

WRF has the possibility to run simulations with different resolutions, both vertical and horizontal. High resolution simulations are more time consuming since the time step for every integration has to be reduced in order to prevent numerical instabilities. The one-dimensional Courant-Friedrichs-Lewy (CFL) condition sets the time step in relation to the grid resolution (see PRESS *et al.* (1992), p.829).

$$C = \frac{u\Delta t}{\Delta x} < C_{critical} \tag{3.8}$$

Where u is the wind speed, Δt the integration time step and Δx the distance between two grid points. Equation (3.8) states that the ratio of Δt to Δx, depending on u, has to be below a certain critical threshold. Furthermore, high resolved domains need essentially more grid points to cover the same area as lower resolution simulations. This is important for example for the inversion of the Laplacian which takes considerably more time for larger matrices. On the other hand it is crucial for the simulation of small scale processes to have a high resolved grid. Therefore, a compromise between the highest needed resolution and least computational time consumption has to be made.

3.8 Postprocessing

For the visualization and data analysis of the model output, the NCAR Command Language (NCL) is used. The advantage of using NCL is that there is already a comprehensive database of example scripts for WRF users.

3.8.1 Interpolation to z-coordinates

One possibility to visualize WRF-output data is making vertical cross sections. For this purpose NCL has an intrinsic function called *wrf_user_intrp3d*. This function interpolates 3-dimensional fields to 2-dimensional vertical cross sections or 2-dimensional horizontal plots at a given height. Vertical cross sections need a 3-dimensional variable as input, a start and end point and a vertical coordinate to which the input data is supposed to be interpolated. We chose the height as vertical coordinate. Note, that the height itself is already an interpolated variable. There is another intrinsic function called *wrf_user_getvar* which calculates the height based on η-levels. Therefore, the new height coordinate is not yet equidistant, since a certain height coordinate is just the height of an η-level. Thus, for our model runs the lowest level is not at 0m but at 19m which corresponds to the lowest η-level in the cross section. The *wrf_user_intrp3d* function first interpolates this non-linear height coordinate to a height coordinate with constant increment. We chose 40m as the distance between to height levels. Afterwards, the 3-dimensional variables which we want to plot are interpolated to this equidistant vertical coordinate. The lowest plotting level is at 40m, because the lowest and second lowest η-levels are at 19m and 56m, respectively. This fact will appear as a white stripe between 0 and 40m in all NCL plots.

Chapter 4

Results of the Case in 1984

The WRF model was used to reproduce the observation of an ice edge jet presented in SHAPIRO and FEDOR (1989). They report about the Arctic Cyclone Expedition (ACE) in 1984 with a focus on boundary-layer fronts, heat fluxes and polar low development. Two transects on 14 February 1984 were taken with a NOAA WP-3D (P-3) research aircraft. The flight started at 1000 GMT in Bodø and headed towards Svalbard. The first transect was south-north aligned. The sea ice edge was crossed at around 75°N. The second transect was in the south west of Svalbard and southwest-northeast aligned (Figure 4.1). The observation of the low-level jet stream was on the latter flight (Figure 4.2). The maximum measured wind speed was about 30 m/s and from a northwesterly direction. The location of the wind maximum was slightly ice inwards and at 870 hPa with a strong boundary layer front beneath and a strong inversion above. The authors compare this setting to a tropopause folding event (see section 2.5). In the case from 1984, however, the frontal zone is created by differential heating instead of a folding down of the tropopause. The air over the sea ice is radiative cooled due to the low temperatures of the ice. The air over the ocean is heated by the relative warm ocean. This difference in surface fluxes of sensible heat is causing the strong front at the ice edge. We showed in section 2.5 that high PV is connected to strong potential temperature gradients. Figure 4.3 illustrates the potential vorticity of

the flow in the observations by SHAPIRO and FEDOR (1989). High PV is found to the east of the wind maximum, which corresponds to the characteristic of the tropopause folding where a spatial difference between the wind maximum and the PV maximum is existent as well. Thus, even if the characteristics of the PV and wind fields are influenced by differential heating, the explanation of jet streams due to tropopause folding can probably also be applied for the 1984 case.

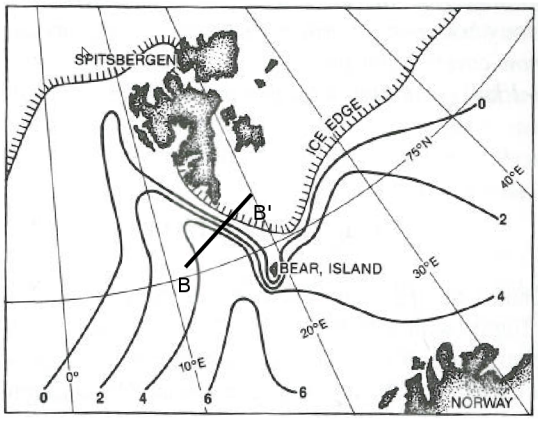

Figure 4.1: Overview of the transect made by SHAPIRO and FEDOR (1989). Adapted from Figure 1 in SHAPIRO and FEDOR (1989)

In order to reproduce the results by SHAPIRO and FEDOR (1989), the WRF model was run. The model run starts at 12 February 1200 UTC. This means that there is more then two days spin up time, which was suggested by the lead author of the SHAPIRO and FEDOR (1989) paper. Figure 4.2 shows a vertical southwest-northeast aligned cross section south of Svalbard (Line BB' in Figure 4.1). A similar cross section based on the WRF model output is shown in Figure 4.5. The position of the cross section is shown together with the sea ice extend (Figure 4.4a) and the sea surface temperature (Figure 4.4b). In comparison to the measurements from the 1984 case, some differences are apparent, especially the location of the sea ice edge is different. The sea ice edge

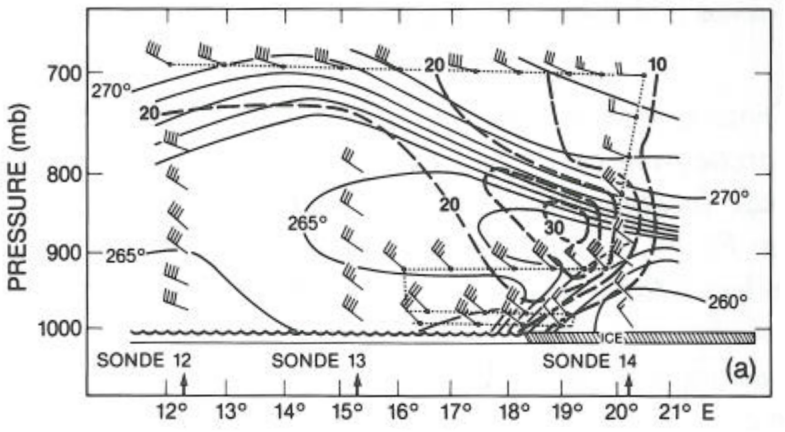

Figure 4.2: Observed low-level jet at the sea ice edge (Figure 6a in SHAPIRO and FEDOR (1989)).

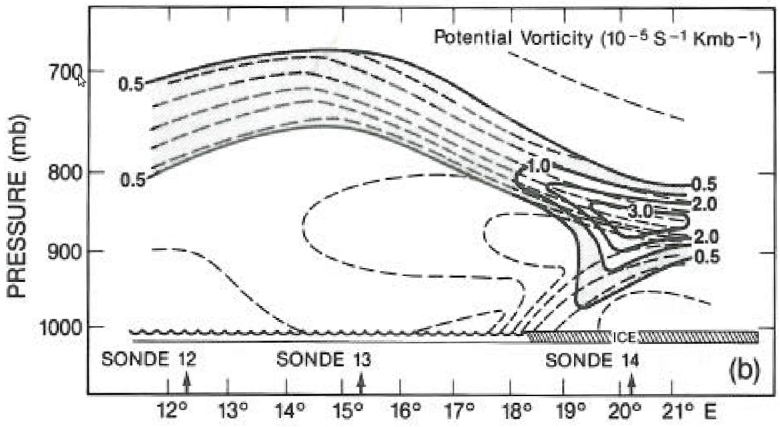

Figure 4.3: Potential vorticity at the sea ice edge (Figure 6b in SHAPIRO and FEDOR (1989)).

is extending almost down to 75° N in Figure 4.1 whereas the sea ice edge in the WRF simulation is making a turn to the east south of Svalbard. Another difference between both studies is the pattern of the sea surface temperature. SHAPIRO and FEDOR

(1989) describe a strong gradient in sea surface temperature of about 4K west of the ice edge. Figure 4.4b has a sea surface temperature difference of only about 2K over the same distance.

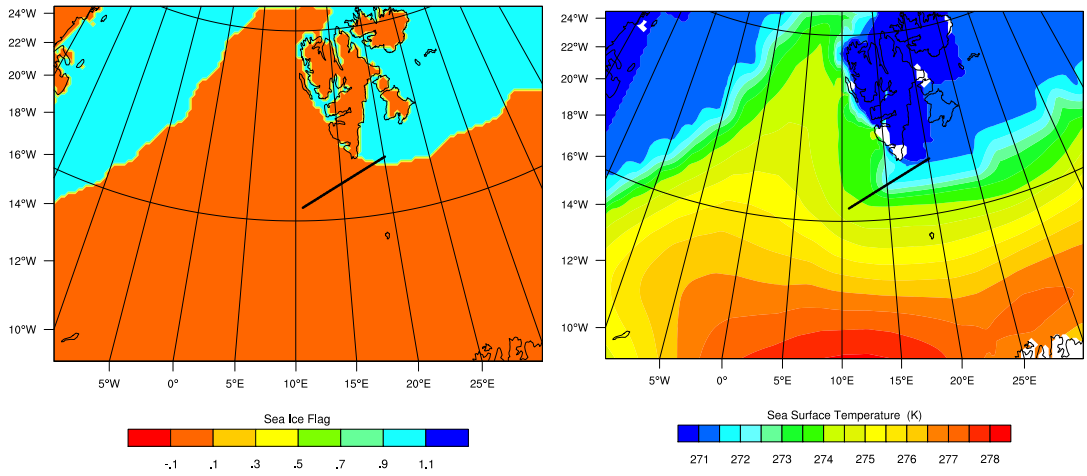

(a) (b)

Figure 4.4: (a) Sea ice extend and (b) sea surface temperature on 14 February 1984 (colors) and position of the cross section (heavy line) in the second domain

No exact time was given for the low-level jet event in the 1984 case by SHAPIRO and FEDOR (1989). Only the take-off time in Bodø was specified, which was 1000 GMT. Figure 4.5 shows the atmospheric situation at 1800 UTC on 14 February 1984. We picked 1800 UTC, because this plot agrees best with Figure 4.2 in comparison to earlier or later times. Here, the total wind speed is plotted, which means,

$$|\vec{v}| = \sqrt{u^2 + v^2} \tag{4.1}$$

There is a total wind maximum of about 30 m/s from northwesterly directions at an altitude of about 2.5km and lies between 16° and 18° East. At around 18° east, a weak boundary layer front is evident which is characterized by a horizontal potential temperature gradient. This marks the transition zone between the sea ice and the open water. West of this front is a rather well mixed boundary layer with decreasing wind

speeds towards the west. This mixed layer is capped by a stably stratified layer. Very weak winds are also found directly above the sea ice.

Differences compared to the jet observed by SHAPIRO and FEDOR (1989) are visible. There is a clear disagreement between the altitudes of the jet. The observed jet is at around 870 hPa, which corresponds to about 1.2 km and lies between the boundary layer front beneath and a strong inversion above. The simulated jet on the other hand is rather within a slightly stable stratification. This reveals the main distinction between the simulation and the measurements. The boundary layer front at the ice edge as well as the strong inversion layer, visible in the flight measurements, are much weaker in the simulation. One reason might be the location of the sea ice edge. The ice edge extends further west in the observations. When looking at Figure 4.2 there are about 17.5 m/s northwesterly winds close to the surface. The ice edge in the simulation with WRF is further east and lies in the southeast of the tip of Spitsbergen. This means that the ice edge is more shielded against winds from the northwest. Indeed, the wind speed is only about 7.5 m/s west of the ice edge.

Another reason is the weaker sea surface temperature gradient and the resulting smaller heat input, which influences the height and strength of the boundary layer inversion. In Figure 4.2 the height of the capping inversion is increasing westwards until 15° East, which is congruent with the increasing sea surface temperature until 15° East longitude (Figure 4.1). In contrast, the boundary layer height is decreasing constantly in the simulation (Figure 4.5). Both, the smaller heating from the sea and the lower wind speeds yield a weaker boundary layer front in the simulation and therefore to a difference in the location of the jet. The analysis of the potential vorticity shows the same difference as well. There is also a shift in altitude of the potential vorticity maximum (Figure 4.6). Additionally, the simulated potential vorticity is about half of the measured, which can be explained by the smaller temperature gradient (see Equation (2.32)). The simulation as well as the observations have in common that the vorticity

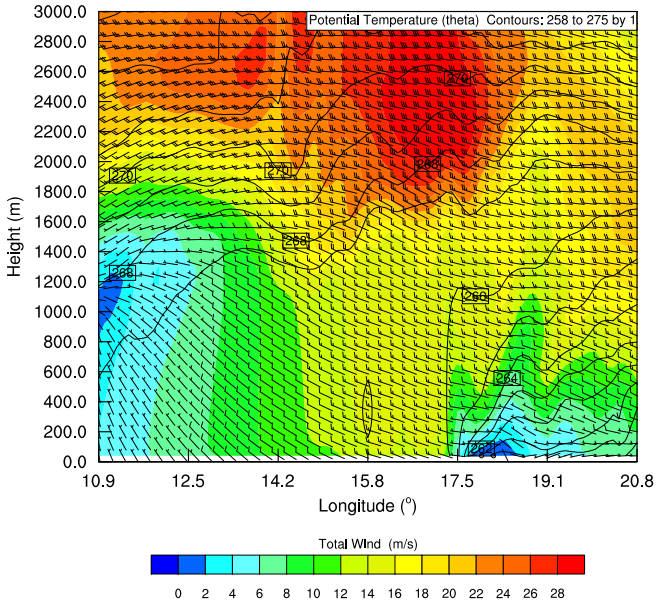

Figure 4.5: Vertical cross section showing the total wind (colors), wind vectors and potential temperature (contours) in the second domain

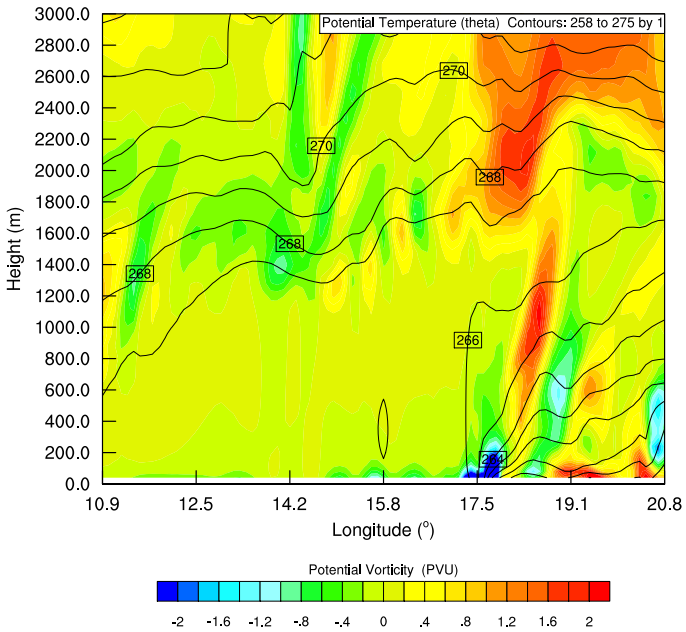

Figure 4.6: Vertical cross section showing the total potential temperature and potential vorticity (contours) in the second domain

maximum is to the east of the jet. However, the WRF simulation has a secondary potential vorticity maximum of comparable strength at 1000 m close to the ice edge. The difference is, that the lower maximum is not connected to a wind maximum which suggests that both maxima are due to different processes.

In conclusion it can be said that the atmospheric conditions described in SHAPIRO and FEDOR (1989) could not be reproduced. This is most likely due to differences in the sea surface temperature and the smaller extend of the sea ice. Also the spin up time of two days is probably too long. After 48 hours the model probably deviates already a lot from the true atmosphere. However, there is indeed a jet of similar strength in the simulation which is, however, probably not due to the ice edge. Therefore this case from 1984 is excluded from further studies here. For a special investigation of this case the original data would have been helpful, but after personal communication with the lead author it is not possible to obtain these data any longer. Another reason to exclude this case was the orography of Svalbard, which likely influenced the generation of the jet together with a rather complicated synoptic situation. The aim of this thesis is, however, to explain low-level jets created only by the differences in temperature between sea ice and open water. So we are looking for cases with frontal zones created only by differences in surface heat fluxes and we demand that no orography or any large scale disturbances interfere with the front.

Chapter 5

Results and Analysis of the Case in 1993

The WRF model was also used in order to reproduce the simulated ice edge jet presented in GRØNÅS and SKEIE (1999). The main emphasis in this paper is on a case where a Norwegian coast guard ship observed wind speeds greater than 32 m/s without any warning given. In order to gain insight about the processes causing such strong winds they used the Norwegian limited area model (NORLAM). The authors explain this strong wind event by a merging of a low-level jet connected to a shallow boundary layer front and a wind maximum associated to an occlusion. A minor point at the end of this article is about a boundary layer front at the ice edge, the vertical circulation at this front and a low-level jet connected to the front. There is no detailed analysis of the jet at the ice edge given. A general wind increase due to an approaching occlusion is stated as the reason for the wind maximum. This rather vague interpretation is the starting point for further research.

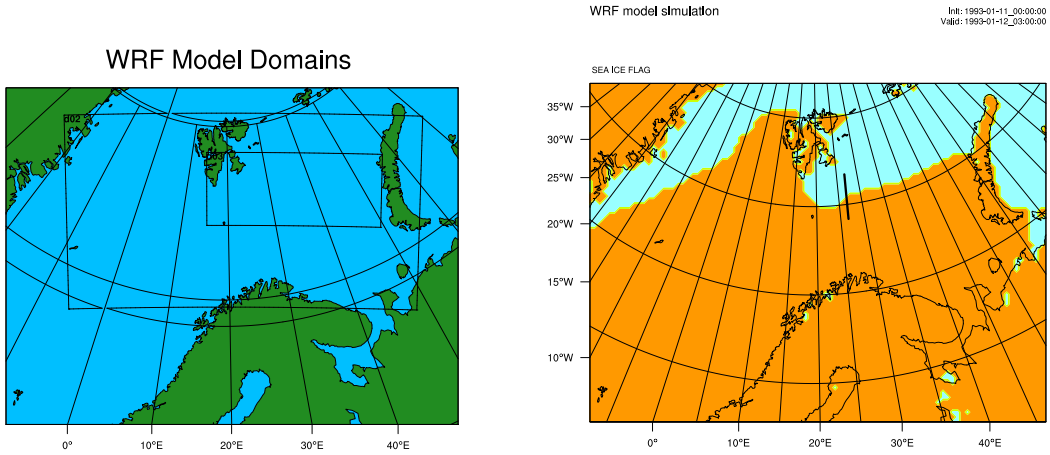

(a) (b)

Figure 5.1: (a) Overview of all three simulated model domains with 27km, 9km and 3km resolution, respectively. (b) The black line is indicating the position of the cross section. The light blue area represents the sea ice.

5.1 Resolution Dependency

The model run starts on 11 January 1993 at 00 UTC, which gives approximately one day spin up time. All the following plots for the 1993 case are from 12 January 1993 at 03 UTC. This is a three hours difference in comparison to the corresponding results presented in GRØNÅS and SKEIE (1999). We chose 03 UTC because at this time the low level jet was at its maximum. WRF was run with three domains with different horizontal resolutions respectively (Figure 5.1a). The setup includes one parent domain and two one-way nested domains. The parent domain has a resolution of 27km, the next finer grid has a resolution of 9km and the resolution in the finest grid is 3km. Three cross sections in each domain were made by using the NCAR Command Language (NCL). All three cross sections range from 77°N to 74°N at 28°E. With these coordinates, the cross sections are about perpendicular to the sea ice edge. Figure 5.1b shows the position of the cross sections and the sea ice extend. Figures 5.2a, 5.2b and

5.2c are showing the total wind and potential temperature in the respective domain. All three plots contain the lower 3km of the troposphere and show similar features. The low level wind maximum is about the same magnitude, which is at around 28 m/s. The location of the jet is at 400 m and slightly ice inward which is valid for all three resolutions. However, the maximum wind speed is varying a little among the three figures. The highest values can be found in Figure 5.2a which has the coarsest resolution. With increasing resolution, the maximum wind speed decreases. The wind pattern above the boundary layer looks similar in all three plots.

Furthermore, there is a difference regarding the potential temperature. In comparison to domain 2 (D02) and 3 (D03), domain 1 (D01) has distinctive kinks in the isentropes. Also does the boundary layer front and the inversion layer look less sharp in Figure 5.2a. The growth of the boundary layer over the open ocean is also much clearer in the domains with 9km and 3km resolution. There, the maximum boundary layer height is growing rapidly up to a maximum of 1200 m. Again, all three plots are consistent above the boundary layer. For further studies, however, we chose D03 with a 3km resolution, because it resolves sharp gradients best, while D01 and D02 revealed distinctive kinks at the sharp fronts.

5.2 Vertical Cross Sections along the Ice Edge

As seen in section 5.1, there is a well defined low level jet close to the sea ice edge. The Figures 5.2a, 5.2b, 5.2c are at a longitude of 28°E, with northeasterly winds, so they show the low level jet at the end of a long fetch along the ice edge (Figure 5.3). It is,however, interesting to see how the jet develops along the edge. Therefore two additional cross section at 35 and 44°E are presented to track the development.

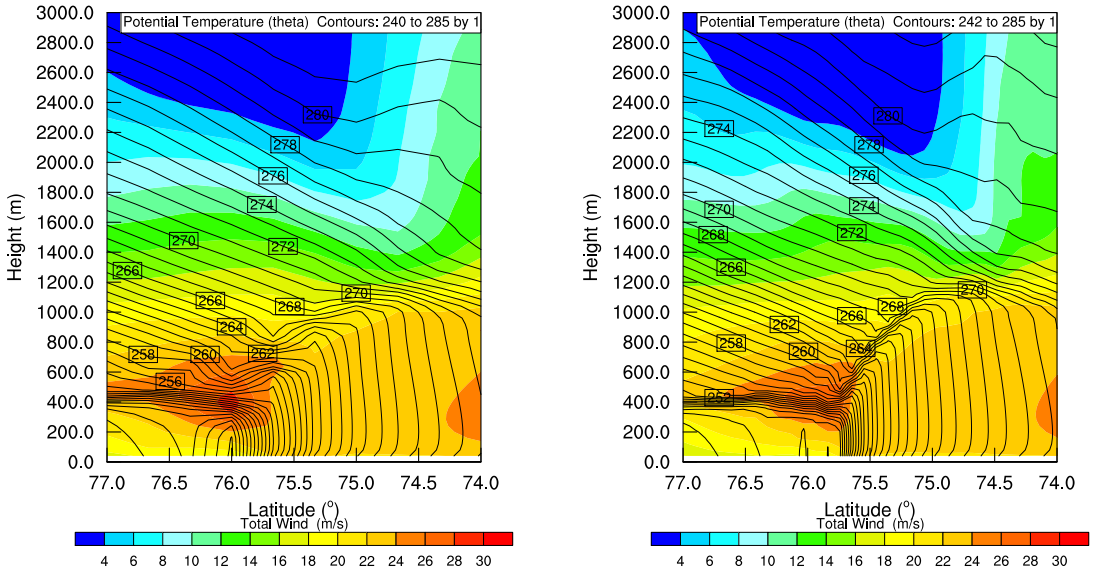

(a)

(b)

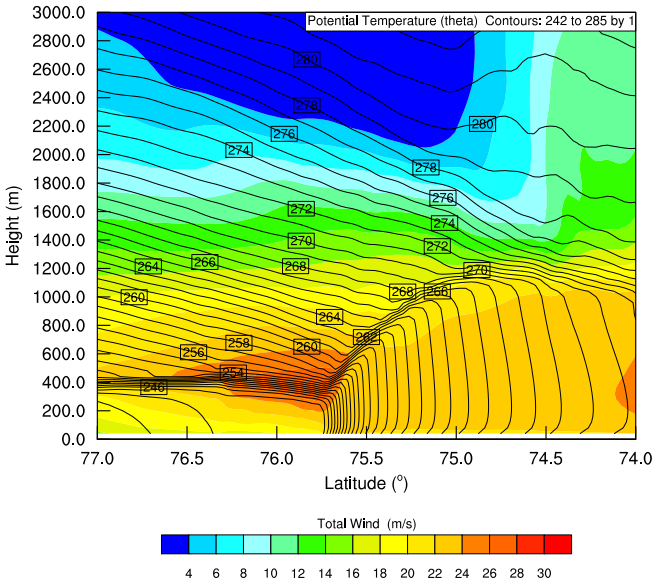

(c)

Figure 5.2: Cross sections from 77°N to 74°N in (a) D01 with 27km resolution ,(b) D02 with 9km resolution and (c) D03 with 3km resolution. The different size of the figures arises from the resolution differences. Colors indicate the total wind and the contours show the potential temperature.

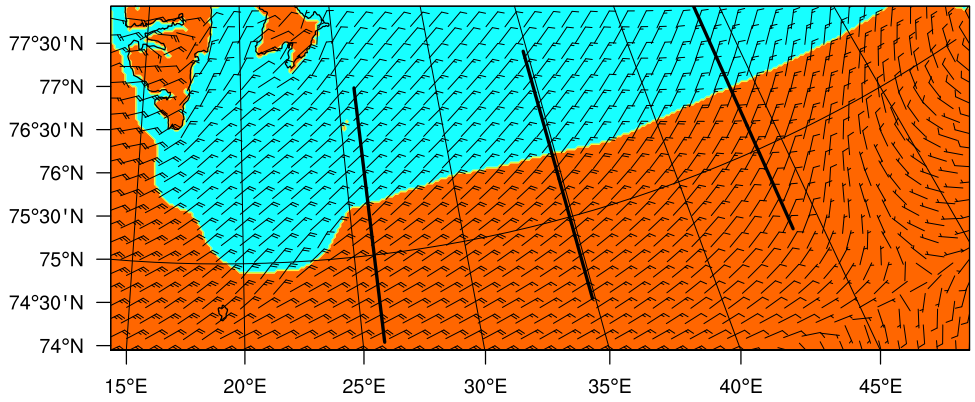

Figure 5.3: Overview of all cross sections. The black lines indicate the position of the cross sections. The light blue shading represents the sea ice.

The most remarkable feature when looking at the three different cross sections is that the jet intensifies with increasing fetch. All three cross sections show the total wind in colors and the potential temperature as contours. At 44°E the total wind has a maximum of about 24 m/s (Figure 5.4). At 35°E the wind maximum has increased to about 26 m/s (Figure 5.5). Also the spatial extend of the jet increases. A further intensification is visible in Figure 5.6 which is the cross section at 26 °E. Here the maximum wind speed exceeds 28 m/s. The wind speed within the boundary layer over the open ocean is also increasing from east to west.

The boundary layer over the ice is stable at all three longitudes and is capped by a strong inversion at 400 m. Over the ocean the boundary layer receives a strong heat input from the surface and hence, the boundary layer height is growing gradually southwards. At 44°E the maximum inversion height is at 800 m and has a gentle slope. On the other hand, the maximum height of the inversion at 26°E is around 1200 m and has a rather steep slope at the transition between sea ice and open ocean. A common feature in all three cross sections is a well-mixed neutral boundary layer.

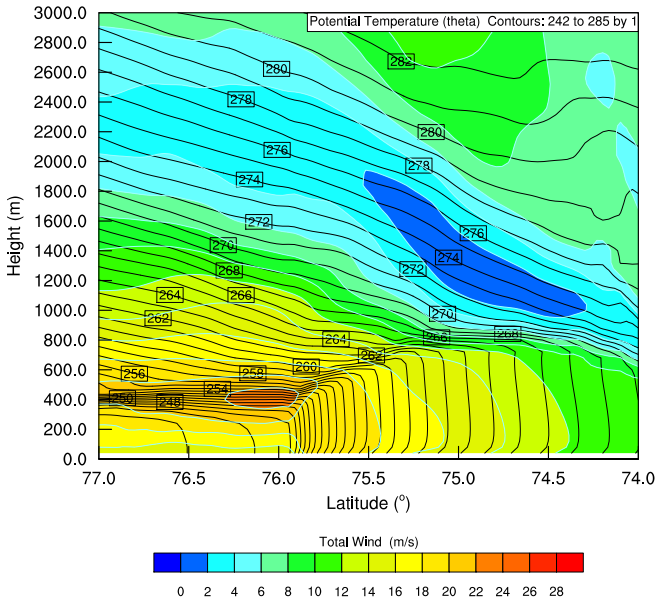

Figure 5.4: Cross section at 44°E. Colors indicate the total wind and the contours show the potential temperature.

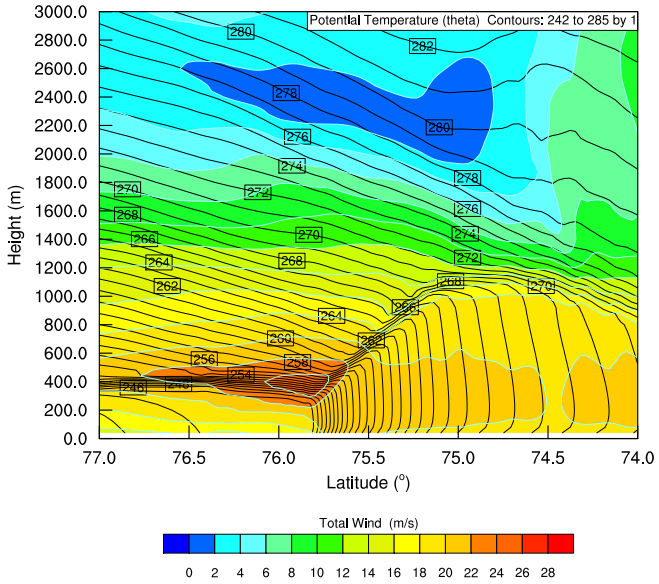

Figure 5.5: Cross section at 35°E. Colors indicate the total wind and the contours show the potential temperature.

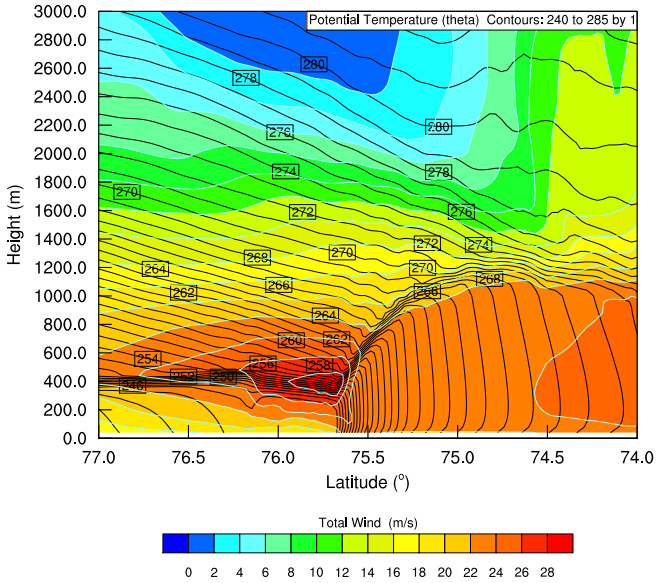

Figure 5.6: Cross section at 26°E. Colors indicate the total wind and the contours show the potential temperature.

Comparing the above mentioned WRF model results with the findings of GRØNÅS and SKEIE (1999) a good agreement is evident. A cross section by GRØNÅS and SKEIE (1999) corresponding to the simulated cross section at 26°is shown in Figure 5.7. Here the full lines indicate the wind along the ice edge and the dashed lines show the geostrophic wind along the ice edge. The ice-ocean border can be found in the middle of the cross section where geostrophic wind values are up to 50 m/s. Like in Figure 5.6 there is a low level jet over the sea ice. The wind maximum reaches 32 m/s which is greater than the maximum in the WRF-simulation. Note, that the Figure 5.7 only shows the along edge wind component whereas Figure 5.6 depicts the total wind speed. To get an impression of how the individual wind components constitute the total wind, an analysis of the edge-along and edge-across component is presented in section 5.4. The geostrophic wind will be analyzed in section 5.5

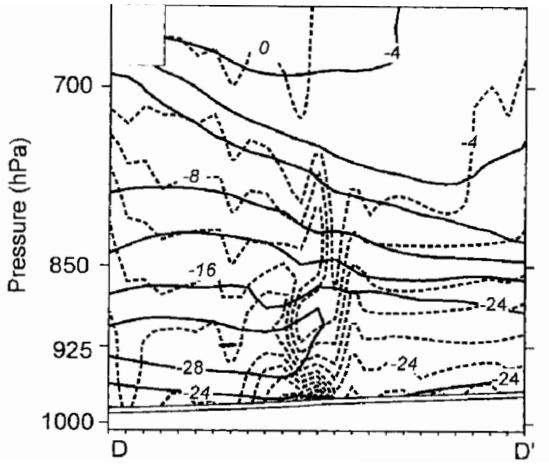

Figure 5.7: North-south cross section from GRØNÅS and SKEIE (1999) (Figure 10c) showing the actual wind along the ice edge (full contours) and the geostrophic wind along the ice edge (dashed contours). Valid at 12 January 1993 00 UTC.

5.3 Horizontal Wind Structures

Figure 5.8 shows a horizontal plot of the total wind speed at 370 m, which is the height of the jet maximum. Higher wind speeds are clearly visible north of the ice edge (indicated by the black line) in a broad band of around 70km. South of the ice edge are the wind speeds 5 to 6 m/s slower, but also here the wind speed increases from east to west. When looking at the 10 m wind (Figure 5.9), the opposite is true. Here the wind speed south of the ice edge is greater than on the northern side of the edge. There is a difference of about 4 to 5 m/s. A comparison of the wind direction at the surface and at 370 m yield a more ice edge parallel wind at 370 m. This right turning of the wind vector with height follows from the Ekman spiral, but it is only seen over the sea ice. The boundary layer over the open ocean is neutral stratified and hence the momentum exchange by vertical fluxes is enhanced, which in turn leads to a more homogeneous vertical distribution of the wind field. The wind at 370 m over the ocean is still within this well mixed boundary layer, as the boundary layer is growing really fast over the ocean. So the wind speed and direction are similar at the surface and at 370 m. A more detailed analysis of the single components of the wind speed is given in the next section

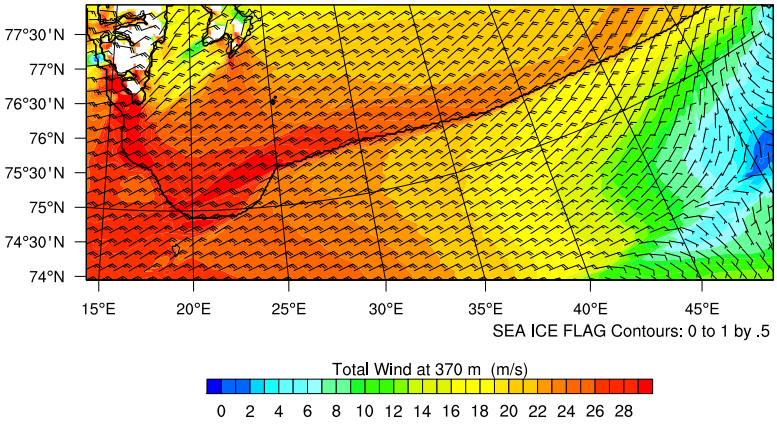

Figure 5.8: Total Wind Speed at Model Level 9 which corresponds to about 370 m. The black line indicates the position of the ice edge.

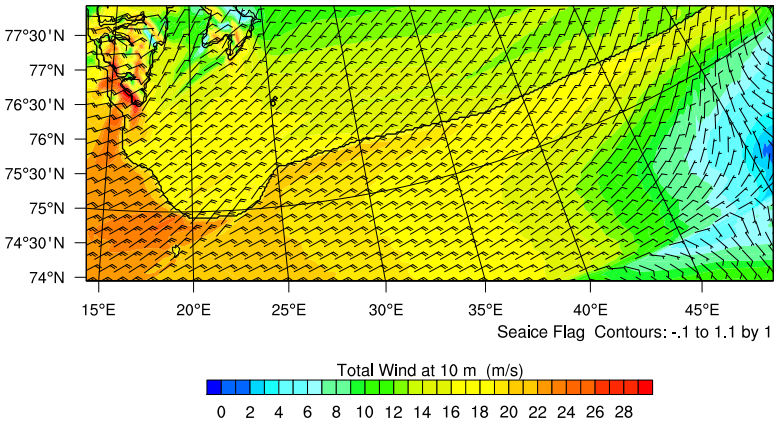

Figure 5.9: Total Wind Speed at 10m. The black line indicates the position of the ice edge.

5.4 Edge-along and edge-across Wind Components

We present east-west and south-north aligned cross sections of the individual wind components along and across the ice edge, with the aim to increase the understanding of the development of the low level jet. The u and v components from the WRF-output

file where rotated to the according cross section by using a rotation matrix (5.1) as it is used for coordinate transformation. The angle of rotation (γ) is obtained by calculating the deviation of the cross section relative to the model grid.

$$\begin{aligned} v_{along} &= \quad \cos(\gamma) * u + \sin(\gamma) * v \\ v_{across} &= -\sin(\gamma) * u + \cos(\gamma) * v \end{aligned} \tag{5.1}$$

Both individual components add up to the total wind.

$$|\vec{v}_{total}| = \sqrt{v_{along}^2 + v_{across}^2} \tag{5.2}$$

The position of the east-west cross section together with the surface wind vectors are shown in Figure 5.10. Here the cross section is about 1500km long and extends from 75°N 15°E to 76°N 50°E and is just over the sea ice. At the western end, the cross section crosses the ice edge perpendicularly.

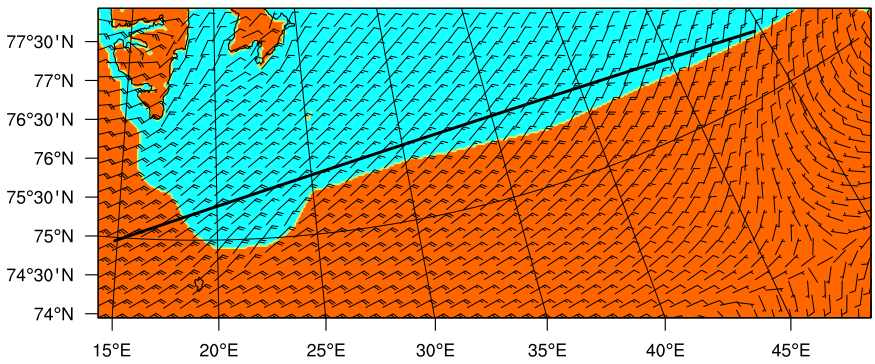

Figure 5.10: The black line indicates the location of the east-west cross section.The wind barbs depict the wind speed and wind direction. The light blue shading represents the sea ice.

Figure 5.11 describes the intensification of the jet from east to west already seen in section 5.2 but with respect to the total wind. Now it can be clearly seen that rather the wind speed along the ice edge increases than the across component (Figure

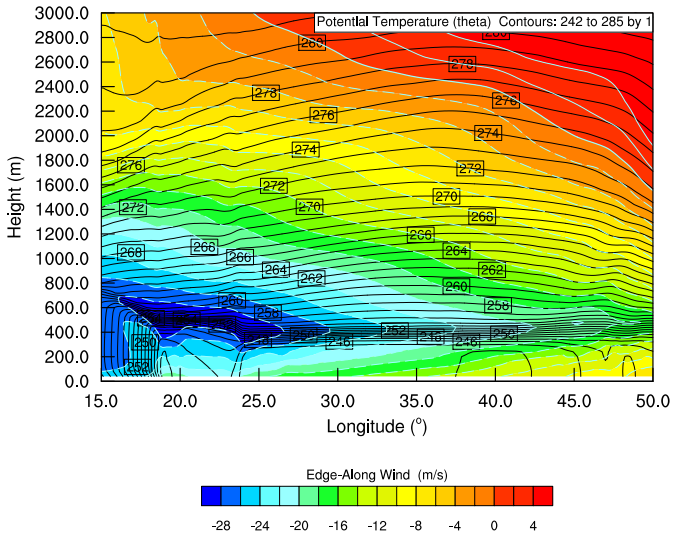

Figure 5.11: Colors indicate the wind along the ice edge in the east-west cross section and the contours show the potential temperature.

5.12). At around 50°E the wind speed along the the ice edge is about 15 m/s and directed toward west. Further downstream at around 26°E, which corresponds to the position of the cross section in Figure 5.6, the wind is increased to around 28 m/s. The largest acceleration is found within the inversion layer at around 300 m to 500 m. On the other hand, the wind across the ice edge within the boundary layer is rather constant around 8 m/s (Figure 5.12). The increased edge-across wind speeds in the east of the cross section are due to a low pressure system in this area. Over the whole cross section the wind in the boundary layer is from northerly directions, which implies off-ice wind conditions and suggests that very high surface sensible heat fluxes exist over the sea (see section 5.6). At the very west of this cross section the boundary layer is very similar to the one seen in section 5.2. The reason is that at this location, the ice edge is south-north aligned and therefore an off-ice flow is existent which leads to a rapid growth of the boundary layer height due to large heat fluxes (see section 5.6).

The south-north cross section in Figure 5.6 showed a total wind maximum close to the ice edge. The total wind in Figure 5.6 was also separated in an edge-along

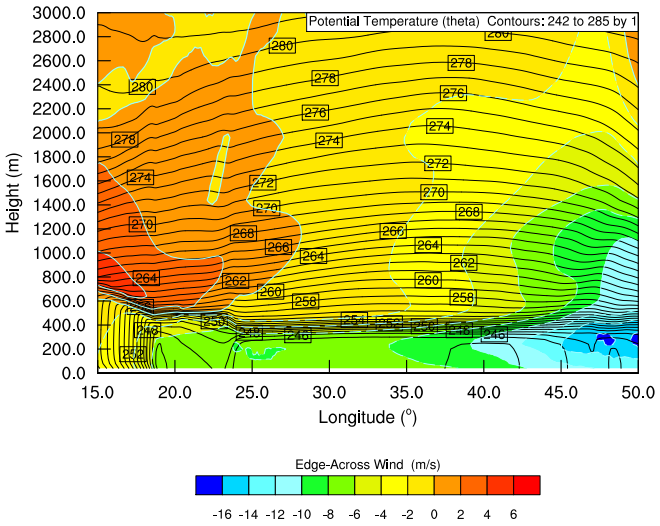

Figure 5.12: Colors indicate the wind across the ice edge in the east-west cross section and the contours show the potential temperature.

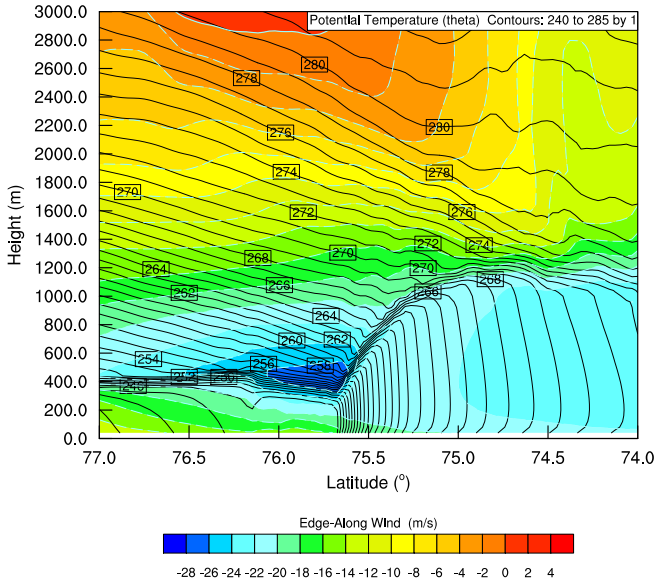

Figure 5.13: Colors indicate the wind along the ice edge in the south-north cross section and the contours show the potential temperature.

and edge-across wind component. The edge-along wind component is shown in Figure 5.13 and the edge-across component is shown in Figure 5.14. The analysis of the individual components shows that the largest part of the total wind is an along ice-edge

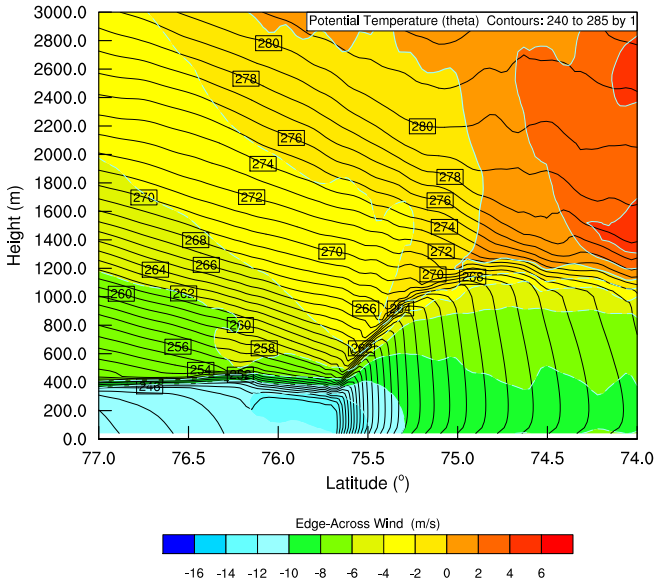

Figure 5.14: Colors indicate the wind across the ice edge in the south north cross section and the contours show the potential temperature.

wind component. The across wind component is between -4 to $-6\,\mathrm{m/s}$ whereas the edge-along component is about $-26\,\mathrm{m/s}$. Negative values indicate flow to the south and to the east, respectively. Figure 5.13 has largest wind speeds within the boundary layer that are decaying above. At 3000 m the wind decelerated to $0\,\mathrm{m/s}$. Over the sea ice and within the boundary layer the wind is also decaying. This is due to slightly stable conditions and friction at the ground. Over the ocean the boundary layer is much deeper and well mixed, so the horizontal momentum can easily be transferred downwards. At a height between 1300 and 1600 m, there is a layer with only little changes in the meridional direction. This suggests that this layer is not within the boundary layer anymore and that surface properties do not influence this layer. The edge-across wind component has its maximum within the boundary layer over the sea ice and close to the ice-edge (Figure 5.14). Thus, the flow shoots off the ice and the high momentum flow is mixed within the deep boundary layer which decelerates the flow. An interesting feature is the reversed flow above the capping inversion over the ocean. There the wind is from southerly directions, whereas underneath the inversion

layer the wind is from northerly directions. The 0 m/s line is drawn in Grey. Above the boundary layer the edge-across wind is also smaller than within the boundary layer.

5.5 Geostrophic Analysis of the 1993 case

GRØNÅS and SKEIE (1999) compared the wind along the ice edge with the edge-along geostrophic wind (Figure 5.7). A strong temperature gradient of 13K across 25km can be found just at the sea side of the ice edge. The resulting pressure gradient corresponds to a geostrophic wind of up to 50 m/s close to the surface (GRØNÅS and SKEIE (1999)). On the other hand, Figure 5.7 shows that the actual wind at the ice edge is about 24 m/s. So the geostrophic wind is about double the actual wind, therefore the flow close to the surface at the ice edge is highly ageostrophic. At the position of the low level jet the situation is somewhat different. Away from the surface and away from the edge, the geostrophic wind is rapidly decreasing, so that the geostrophic wind at the low level jet location is just around -20 m/s. The actual wind at this position is at its minimum , which means values of around -32 m/s. Note that minimum does not mean lowest absolute values, but rather a maximum in easterly or northerly winds. Thus, the actual wind is super-geostrophic. Higher up, the patterns of both winds become more similar, however, the actual wind is still 4-8 m/s faster.

5.5.1 Geostrophic wind in η-coordinates

Similar to the geostrophic analysis in GRØNÅS and SKEIE (1999), the WRF output was also tested in terms of geostrophic wind. The calculation of the geostrophic wind components were made according to section 3.4. The presented cross section is at 26°E and extends from 77°N to 74°N which is the same as in Figure 5.6. Figure 5.15 shows the geostrophic wind and the actual wind along the ice edge.

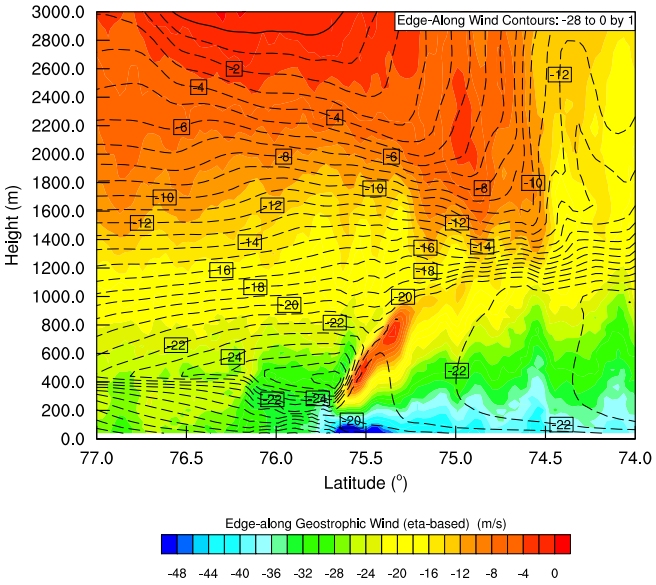

Figure 5.15: South-north cross section at 26°E showing the actual wind along the ice edge (contours) and the geostrophic wind along the ice edge (colors).

Above the boundary layer, both winds are in good agreement, this applies to both, the pattern as well as the absolute values. The actual wind also features the dip of the geostrophic wind between 74.5°N and 75.2°N. However, two clear spots where the actual wind deviates from the geostrophic balance can be detected. The most prominent is just at the sea ice edge at the surface. Another remarkable feature is at the sloped capping inversion south of the low level jet. Here, the geostrophic wind is rapidly slowing down to 0 m/s. The ageostrophic wind, which is the difference between the actual wind and the geostrophic wind is shown in Figure 5.16.

The ageostrophic wind is, for the most part above the boundary layer, between -4 and 4 m/s. There are some patches with an ageostrophic wind component up to 8 m/s. Within the boundary layer, the ageostrophic wind is generally increasing toward the surface which results from frictional processes. The maximum absolute values are larger over the ocean (≈ 20 m/s) than over the sea ice (≈ 16 m/s). The strongest

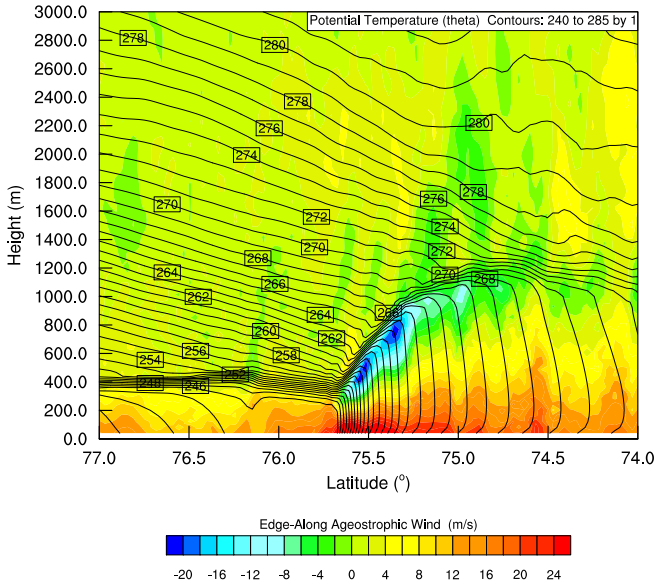

Figure 5.16: South-north cross section at 26 °E showing the ageostrophic wind along the ice edge (colors) and the potential temperature (dashed contours).

ageostrophic wind is found close to the edge at the surface, whereas the absolute minimum is found just below the sloped capping inversion. There, values are exceeding 24 m/s and −20 m/s, respectively. These extrema are accounting for the not slowing down of the actual wind in comparison to the geostrophic wind. The actual flow cannot slow down that fast over a such a short distance due to its inertia. Furthermore, the used boundary and surface layer schemes are probably not very accurate at the ice edge. Within the boundary layer over the sea ice, the geostrophic wind is staying rather constant, whereas the actual wind is decreasing gradually toward the surface. The opposite happens in the boundary layer over open ocean. The actual wind is nearly constant throughout the boundary layer, but on the other hand, the easterly geostrophic wind increases toward the surface.

The major finding, however, is that the low level jet is indeed in geostrophic balance. South and below the low level jet, the geostrophic wind is influenced by the strong temperature gradients and rapidly slows down. Towards north, both, the geostrophic wind

and the actual wind slow down as well. Above the local wind maximum, the geostrophic wind is slowing down. As Figure 6.12 shows, the isentropes above the boundary layer are tilted. This causes a thermal wind which is responsible for the slow down of the geostrophic wind. Thus, we hypothesize that the prominent low level jet is rather an effect of a slowing down of the surrounding air masses than an increased wind speed at this particular location.

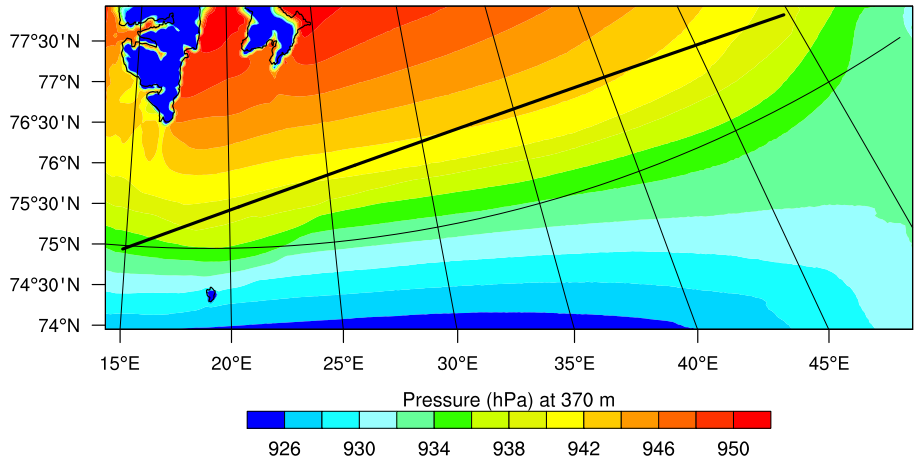

Figure 5.17: Horizontal plot showing the pressure at 370 m, which corresponds to the low level jet height. The black line indicates the location of the east-west cross section.

The accordance of the low level jet with the geostrophic wind can also be supported by recalling Figure 5.11. This plot described an acceleration of the actual wind along the ice edge (see Figure 5.17 for the position of the cross section). Note that the cross section in Figure 5.11 was slightly ice inward. However, Figure 5.15 showed that the actual wind at the jet position, which is slightly ice inwards, was not affected by the ice edge. Therefore we would expect that the actual wind as well as the geostrophic wind are in accordance with the large scale pressure gradient. Figure 5.17 shows the atmospheric pressure at 370 m which corresponds to the low level jet height. Indeed, the meridional pressure gradient increases from east to west which would lead to an increase of the geostrophic wind.

The geostrophic wind together with the actual wind along the ice edge is depicted in Figure 5.18, which is an east-west cross section. At around 400 m height the speed of the along-edge wind is gradually increasing from east to west and also the geostrophic wind is increasing. This agrees very well with the above shown pressure distribution at this height. The ageostrophic wind along the ice edge at 400 m height is about -4 m/s (Figure 5.19), which confirms the good agreement of geostrophic wind and edge along wind. However, the ageostrophic wind reaches a maximum within the boundary layer and a minimum above the boundary layer at around 23°E. It is there, where the sea ice edge makes a turning toward the south, so the geostrophic wind is flowing rather perpendicular toward the inversion layer. Obviously, the strong temperature gradients are influencing the pressure field to a large extend resulting in a complex geostrophic wind pattern.

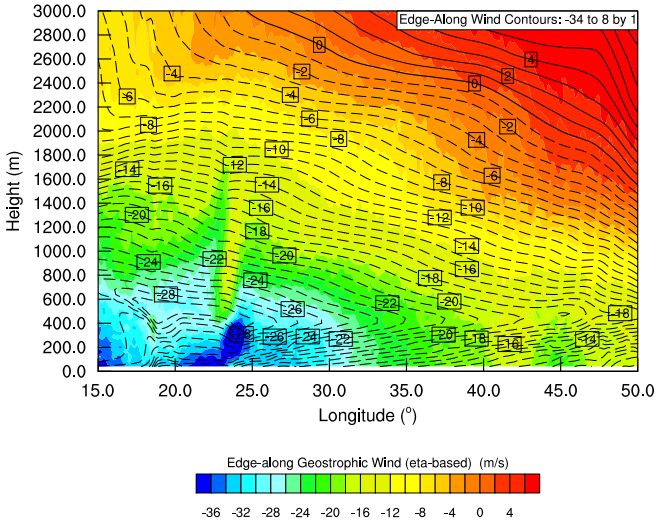

Figure 5.18: East-west cross section, depicted is the edge-along geostrophic wind (colors) and the actual edge-along wind (dashed contours).

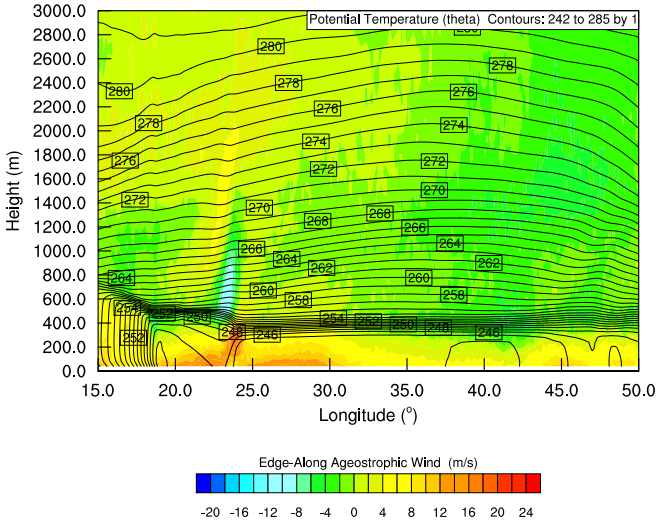

Figure 5.19: East-west cross section, depicted is the edge-along ageostrophic wind (colors) and the potential temperature(dashed contours).

5.5.2 Geostrophic wind in z-Coordinates

The geostrophic wind in z-coordinates is given by (2.5) in section 2.1. The interpolation from the model output variables defined on η-levels to a z-coordinate system is described in section 3.8.1. The calculated geostrophic wind in z-coordinates is shown in Figure 5.20. For comparison purposes, the geostrophic wind on η-levels together with the potential temperature is shown in Figure 5.21.

Comparing the geostrophic wind in z-coordinates with the geostrophic wind in η-coordinates reveals a good agreement. As explained in section 2.4, the geostrophic wind increases eastwards whenever there is a negative meridional potential temperature gradient. Figure 5.20 shows as a decreasing westward geostrophic wind with height above the boundary layer. There, the potential temperature increases from north to south, which is the prerequisite for an eastward directed thermal wind. Within the boundary layer, Figure 5.20 also exhibits the two prominent features which are visible in Figure 5.21 as well.

The difference between the geostrophic wind in both coordinate systems is plotted in Figure 5.22. The difference is mainly between $\pm 1\,\mathrm{m/s}$. Only at the ice edge where a

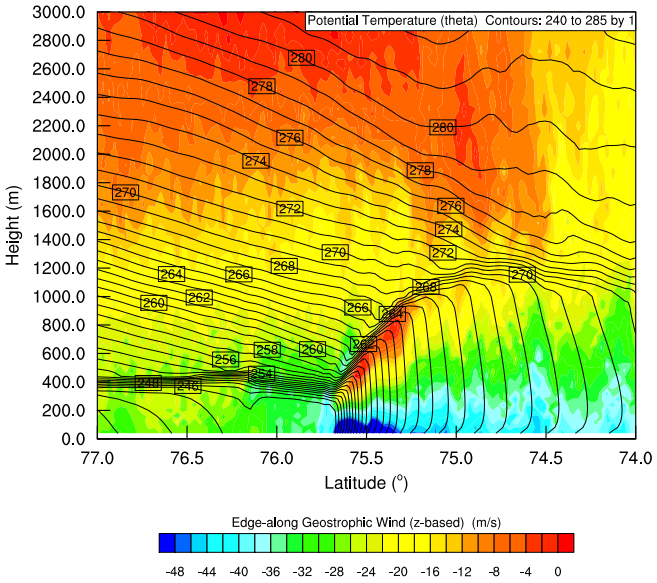

Figure 5.20: South-north cross section at 26°E showing the geostrophic wind along the ice edge based on z-coordinates (colors) and the potential temperature (contours).

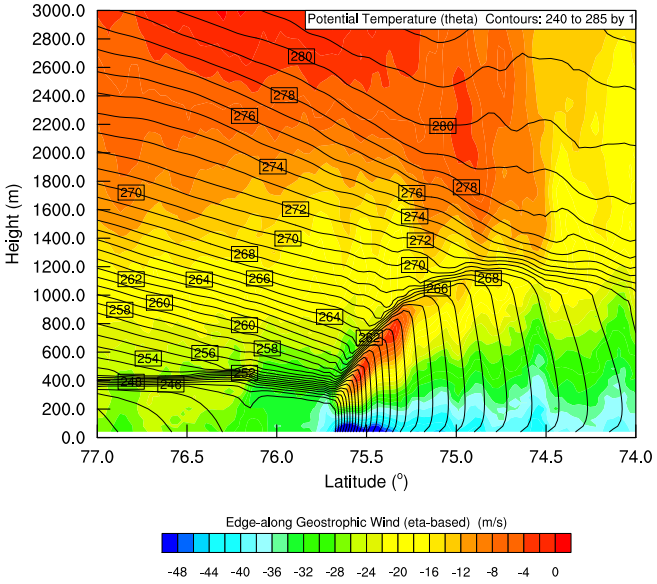

Figure 5.21: South-north cross section at 26°E showing the geostrophic wind along the ice edge based on η-coordinates (colors) and the potential temperature (contours).

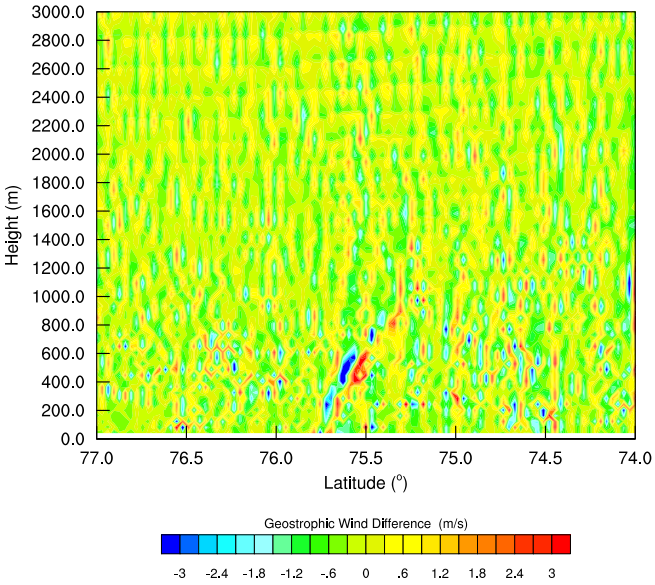

Figure 5.22: South-north cross section at 26°E showing the difference between the geostrophic wind based on z-coordinates and the geostrophic wind bases on η-coordinates.

strong shear of the geostrophic wind appears, the values are between $\pm 3\,\mathrm{m/s}$. There, interpolation errors have the largest effect due to the large difference between the geostrophic wind south and north of the sloped inversion. These results lead to the conclusion that the computation of the geostrophic wind in z-coordinates is reasonable when there are no strong potential temperature gradients existent.

5.5.3 Thermal Wind

The strong minimum in geostrophic wind at the surface close to the ice edge is caused by the large temperature differences between the radiative cooled air over the sea ice and the heated air over the ocean. This large temperature difference across the edge sets up a large pressure difference at the surface. At the cold side the surface pressure is relatively high and on the warm side of the edge the surface pressure is relatively low, which leads to an ageostrophic flow from high to low pressure. This ageostrophic flow accelerates the geostrophic wind toward the west (see chapter 2). The strength of the

geostrophic wind exceeds 50 m/s. The thermal wind was calculated based on (2.29) and is plotted in Figure 5.23. The negative meridional temperature gradient at the surface causes a thermal wind, which accelerates the geostrophic wind with height toward the east until is reaches a maximum of 0 m/s just below the boundary layer inversion. This means, within about 500 m the geostrophic wind changes from over −50 m/s to 0 m/s which corresponds to a vertical wind gradient of about 0.1/s. Large values around 0.2/s are found directly at the ice edge, which is in the same order of magnitude as the approximation made above (0.1/s). Large positive thermal wind values confirm the eastward increase of the geostrophic wind with height, shown in Figure 5.23. However, above the boundary layer a geostrophic wind of about −25 m/s is found. In order to decrease the geostrophic wind from around 0 m/s just below the capping inversion to values of −25 m/s, a strong thermal wind is needed. A westward increase of the geostrophic wind with height can only be realized by a positive meridional temperature gradient. This is the reason why the capping inversion has such a steep slope at the ice edge. The geostrophic wind has to decrease over a very short distance and thus, the temperature gradient has to be reversed.

Concluding the geostrophic analysis, it has to be emphasized that the generation of the low level jet at the ice edge described in GRØNÅS and SKEIE (1999) and modeled by WRF is not directly related due to the ice edge. Rather, the adjacent air masses are affected by the thermal wind which exists due to the strong potential temperature gradient at the ice edge.

5.6 Surface Sensible Heat Fluxes

The strong potential temperature gradient, leading to a strong thermal wind, is caused by differential heating across the ice edge. When cold air from over the sea ice is advected over the open ocean, a large temperature difference between air and surface

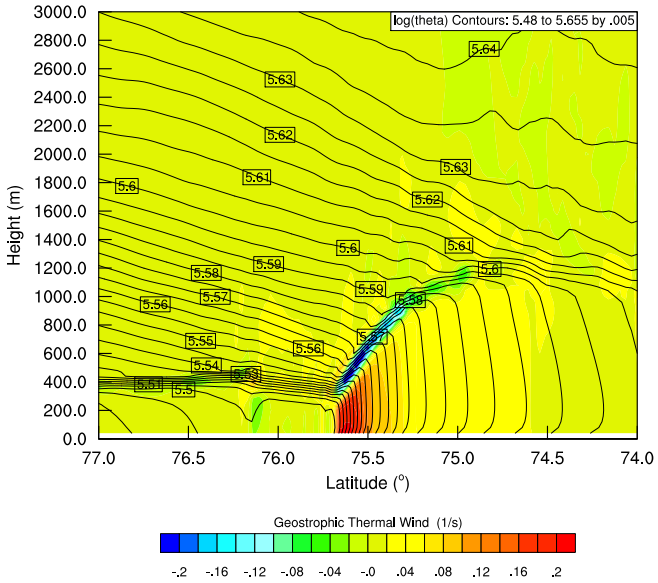

Figure 5.23: South-north cross section at 26°E showing the thermal wind based on z-coordinates (colors) and the logarithm of the potential temperature (contours).

temperature exists. This leads to large surface fluxes of sensible heat from the ocean to the atmosphere. Over the sea ice the surface sensible heat fluxes are clearly smaller, since the difference between air and surface temperature is much smaller. The upward sensible heat flux at the surface is shown in Figure 5.24. Especially close to the ice edge, where there is a sudden increase in skin surface temperature, extreme values of up to 2000W/m^2 in sensible heat flux appear. The skin surface temperature of the sea ice is at around 248K and the ocean has a skin temperature of around 273K (Figure 5.25). This makes a difference of 25K across a very short distance. Especially under off-ice wind conditions the cold air masses over the ice are exposed to a very warm surface underneath, which leads to very large upward heat fluxes.

A discussion of sensible heat fluxes is also included in GRØNÅS and SKEIE (1999). Their results are displayed in Figure 5.26. Note that the fluxes are defined at around 100 m and not at the surface. Assuming that the surface layer is about 10% of the boundary layer (STULL (1988)), the measurements at 100 m are within the surface

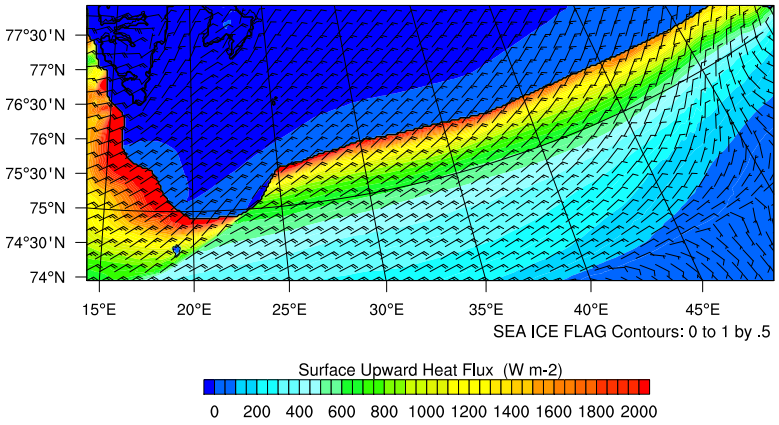

Figure 5.24: The surface upward sensible heat flux is indicated by colors. The wind barbs represent the wind speed and wind direction.

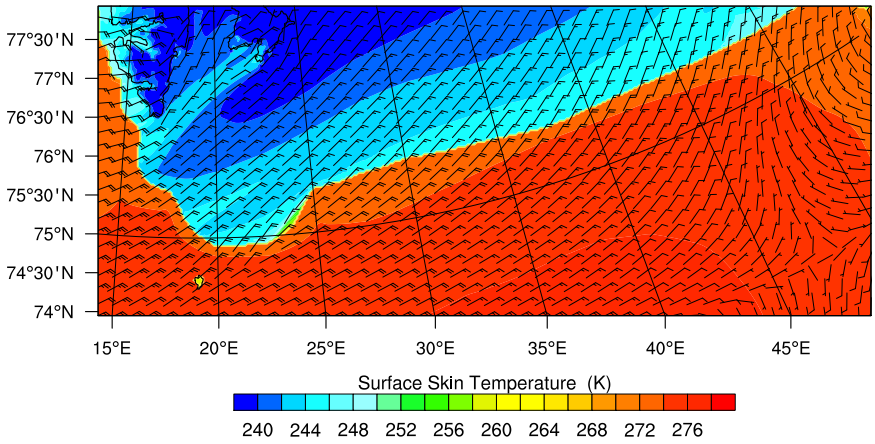

Figure 5.25: The surface skin temperature is indicated by colors. The wind barbs represent the wind speed and wind direction.

layer. The surface layer is also called constant flux layer, because turbulent fluxes vary less than 10% of their magnitude. Thus, the flux measurements at 100 m are comparable with surface fluxes. The simulations by GRØNÅS and SKEIE (1999) also exhibit extremely large values of sensible heat fluxes of up to 1200W/m^2, which is not as high as in the WRF-simulation. The smaller sensible heat flux results from a smaller temperature difference across the ice edge. GRØNÅS and SKEIE (1999) specify the difference to be 13K. Nevertheless, the energy input from the ocean to the atmosphere

is very large and of great importance for generation of the thermal wind. Sensitivity tests regarding the surface sensible heat flux are presented in the following sections. One WRF run with modified surface energy budgets (PolarWRF) and one run entirely without surface fluxes were made. The results from this and the previous sections will be referred to as control run in the following comparisons.

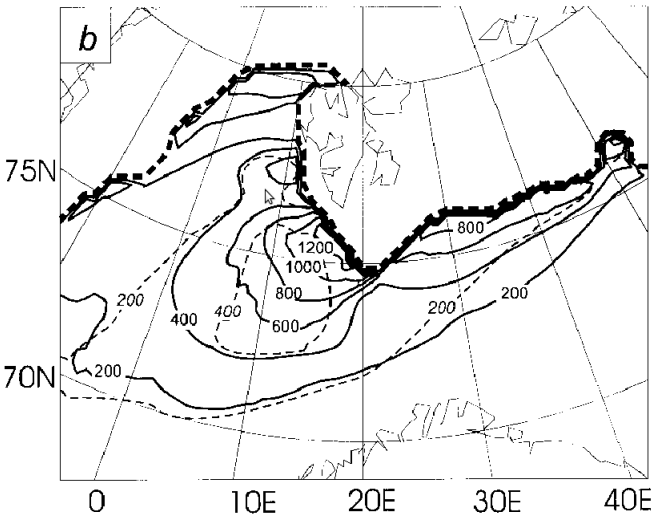

Figure 5.26: Upward Sensible Heat Flux at around 100 m height. Contours show sensible (solid lines) and latent heat (dashed lines) with 200W/m^2 increment. Figure 7b in GRØNÅS and SKEIE (1999)

5.7 PolarWRF Simulations of 1993 Case

The section 5.5.3 reasoned that the strong temperature gradients caused by the very large upward surface sensible heat flux lead to a strong thermal wind. As described in section 5.6, the sensible heat flux at the surface showed values of up to 2000W/m^2. These values seem unrealistic. As mentioned in the introduction, surface sensible heat fluxes over the ocean close to the ice edge may reach values of about 300W/m^2 (PETERSEN and RENFREW (2009)). Therefore a modified version of WRF especially

made for polar environments was used. This version is called PolarWRF and is described in detail in section 3.6.With this modified version of WRF another simulation was run in order get more realistic results. The results of the PolarWRF simulation are shown below. First, Figure 5.27 shows a horizontal plot of the surface sensible heat flux. The absolute values are clearly lower than the values obtained with the regular WRF model (see Figure 5.24), they are about half of the original values. The maximum heat flux is about 1200W/m^2, which is in good agreement with the heat fluxes obtained by GRØNÅS and SKEIE (1999) (Figure 5.26). The values south of the east-west aligned ice edge southeast of Svalbard are about 800W/m^2. This fits also very well with the results by GRØNÅS and SKEIE (1999). However, heat fluxes of up to 1200W/m^2 are probably still too large and introduce too sharp temperature gradients.

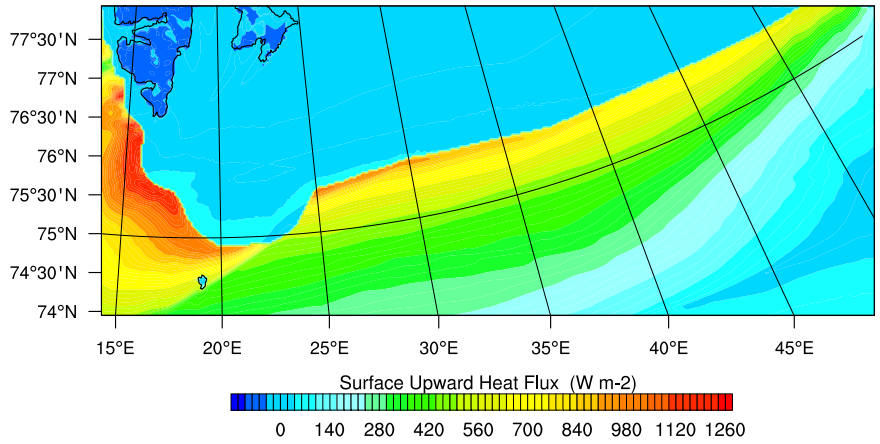

Figure 5.27: The upward surface sensible heat flux from the PolarWRF simulation is indicated by colors.

The modifications in the PolarWRF version are also influencing the wind. A cross section similar to Figure 5.6 was made. Figure 5.28 shows the total wind together with the potential temperature. As expected, the potential temperature gradients are not that strong as they were in the regular WRF run. We showed that the sloping capping inversion is due to the strong potential temperature gradient at the surface hence, the slope of the inversion layer just at the sea side of the edge is less steep. Also, the height

of the inversion layer has decreased. Especially over the sea ice, the boundary layer height is reduced to about 200 m. The total wind speed just above the boundary layer increased a little. Clear changes regarding total wind maximum are visible. North of the total wind maximum, the wind speed increased which is most likely due to the changes of the inversion layer. To the south close to the edge,the wind does not slow down as rapidly as in Figure 5.6. Above the boundary layer, the PolarWRF simulation is comparable to Figure 5.6. The absolute values of the wind speed are about 2 m/s less in the PolarWRF simulation. However, the wind speed pattern looks similar.

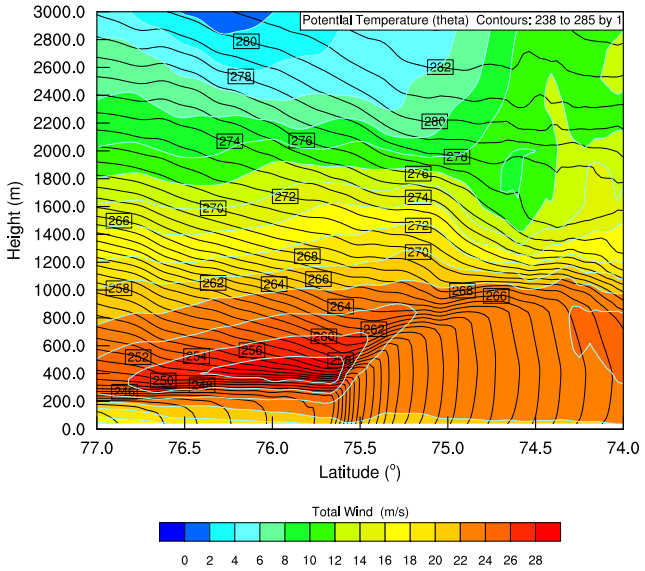

Figure 5.28: South-north cross section at 26°E of the PolarWRF simulation. Colors illustrating the total wind and contours showing the potential temperature

The change of the geostrophic wind in the PolarWRF simulation is shown in Figure 5.29. Whereas the regular WRF had a minimum geostrophic wind of −50 m/s and a maximum of about 0 m/s within the boundary layer, the PolarWRF simulation exhibits a minimum of −46 m/s close to the surface and a maximum of −14 m/s just below the capping inversion close to the ice edge. Figure 5.29 shows lower geostrophic wind speeds over the sea ice. This explains why the total wind maximum in Figure 5.28 was extended toward the north. Following the geostrophic theory the edge-along wind has

to decrease to more negative values which is most likely caused by the changes in the inversion layer. The change of the geostrophic wind with height is shown in Figure 5.30.

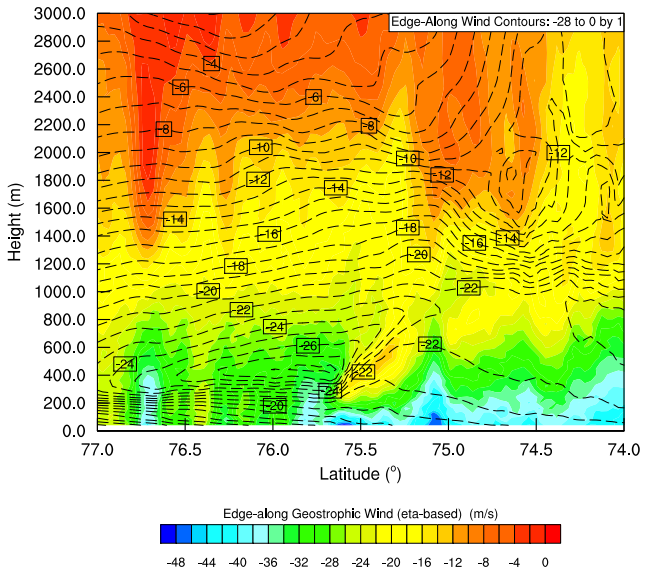

Figure 5.29: South-north cross section at 26°E of the PolarWRF simulation. Colors illustrating the geostrophic wind along the ice edge and contours showing the actual wind along the ice edge.

The thermal wind confirms that the geostrophic wind over the sea ice is decreased due to an altered potential temperature distribution and thus, the total wind speed adapts to these changes. Figure 5.23 has a kink at 76.1°N in the inversion layer, this kink is missing in Figure 5.30 and thus, the geostrophic wind is not slowed down but rather decreased further.

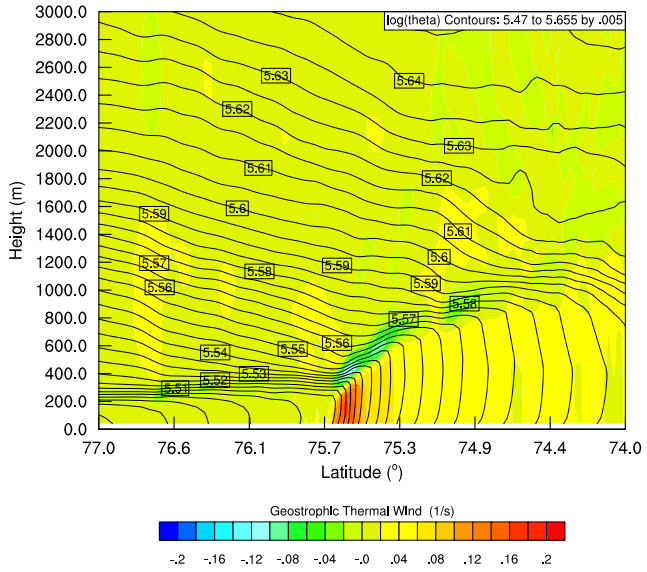

Figure 5.30: South-north cross section at 26°E of the PolarWRF simulation. Colors illustrating the thermal wind based on z-coordinates and contours showing the logarithm of the potential temperature.

5.8 WRF Simulation without Surface Fluxes

Finally, the surface fluxes were completely turned off, where the regular WRF was used again. The run without surface fluxes is onwards called noflux run. The PolarWRF simulations showed that a reduced surface sensible heat flux influenced especially the wind over the sea ice and close to the sloped capping inversion. However, south of the low level jet, the wind is still slowed down. This is a result of the still existent slope of the capping inversion which is due to the strong potential temperature gradient at the surface. We expect from the WRF simulation without surfaces fluxes that the wind maximum seen in Figure 5.6 will not be spatially restricted to the ice edge. The strong potential temperature gradient at the ice edge will not form and therefore the total wind will not be slowed down by the thermal wind. The total wind in the WRF simulation without surface fluxes is shown in Figure 5.31. Note that the range of the color bar has changed. The lacking of surface heat fluxes causes that the strong front at the ice edge is not existent anymore. Thus, the thermal wind is not existent and

therefore, the geostrophic wind is not slowed down. This yields to an increasing total wind toward the south which reaches a maximum at around 74.3°N. An explanation of this maximum is not part of this thesis.

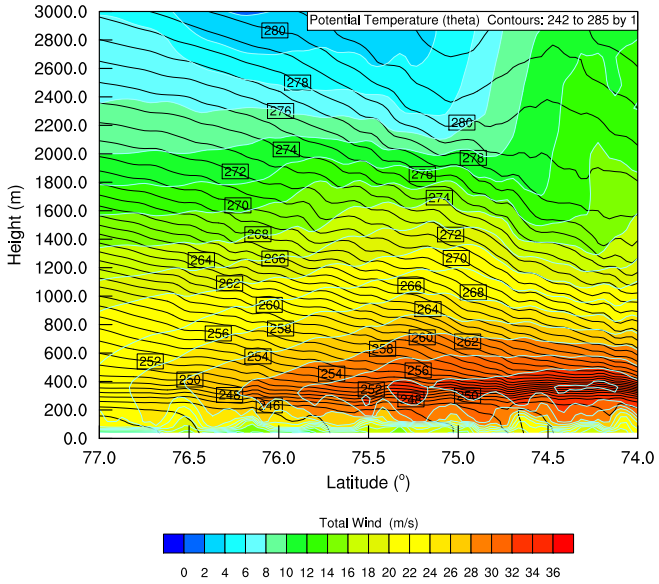

Figure 5.31: South-north cross section at 26°E of the WRF run without surface fluxes. Shown is the total wind (colors) and the potential temperature (contours).

It stands out that the total wind speed at the low level jet position is about 28 to 30 m/s, which are about the same values as in the WRF control run. The difference between the total wind in the control run and the noflux run is shown in Figure 5.32. The difference is made by subtracting the total wind in the noflux run from the total wind in the control run. This means negative values indicate that the total wind is faster in the noflux run than in the control run. The isentropes from the control run are overlaid for better orientation. There is a prominent minimum within the boundary layer over the ocean, which confirms the statement that the wind is slowed down due to the strong potential temperature gradient initiated by the differential heating. The most remarkable feature, however, is the small difference in total wind at the low level jet position which is about -2 m/s. This proofs, that the wind speed at the position of

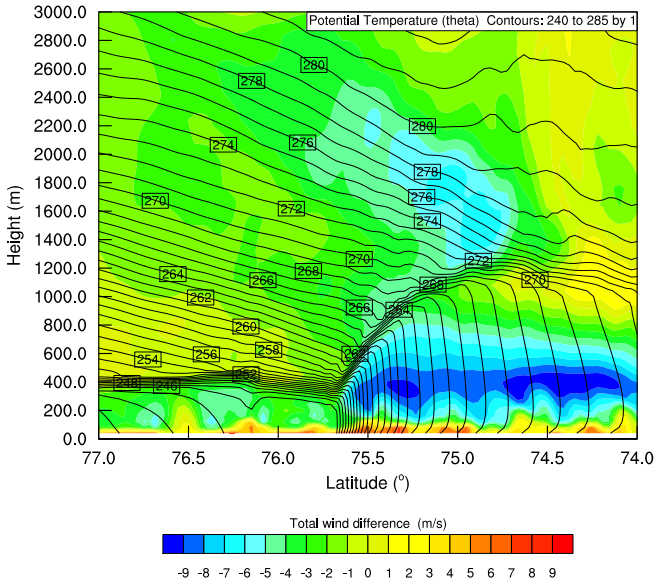

Figure 5.32: South-north cross section at 26°E showing the difference between the total wind based in the control run and the total wind from the simulation without surface fluxes (color). The contours illustrating the potential temperature from the control run.

the low level jet not forced by the ice edge. Without an ice edge, the maximum wind speed would be even higher. The only effect of the ice edge is the slowing down of the wind south of the jet. This supports the results of the geostrophic analysis. The wind maximum seen in Figure 5.6 may not be regarded as a low level jet in a common sense, since the absolute value of the wind maximum is not forced by the ice edge, but rather by the large scale pressure gradient.

Chapter 6

Results and Analysis of the Case in 1997

DRÜE and HEINEMANN (2001) report about aircraft experiments during the Katabatic Wind and Boundary Layer Front Experiment around Greenland in April 1997 (KABEG). This campaign was carried out in the Davis Strait between Baffin Island and Greenland. The main emphasis was on boundary layer fronts with winds parallel to the sea ice edge. The measurements were taken with the POLAR 2, a research aircraft from the Alfred-Wegener-Institut (AWI). In total there were three flights with an U-shaped flight pattern. This included one crossing of the ice edge and two runs parallel to the ice edge with one over the sea ice and one over the open ocean, respectively. Another common feature among the three flights is the synoptic wind from northerly directions close to parallel along the sea ice edge. All three cases were simulated, using WRF. However, in this thesis we only present the WRF run made for the flight on 15 April 1997. The reason is that the other two cases show comparable features at the ice edge and simply that DRÜE and HEINEMANN (2001) describe the event on 15 April in more detail. Figure 6.1 shows the sea ice distribution (colors) and the position of the cross section (black line). The positions of three vertical profiles are indicated by colored crosses. The original flight track flown during the KABEG campaign is shown

in Figure 6.2. Here, the WRF simulation is corresponding to the flight track marked with 1. There is a difference in the position of the cross section made by the use of the model and the cross section of the flight. This is mainly due to the disagreement in sea ice cover between both cases. The open water, east of the sea ice, in the WRF simulation extends only as far north as 65.5°N, whereas the open water in Figure 6.2 can be found at latitudes of up to 68°N. Since we want that the flow covers the same distance parallel along the ice-edge, the cross section in Figure 6.1 is further south.

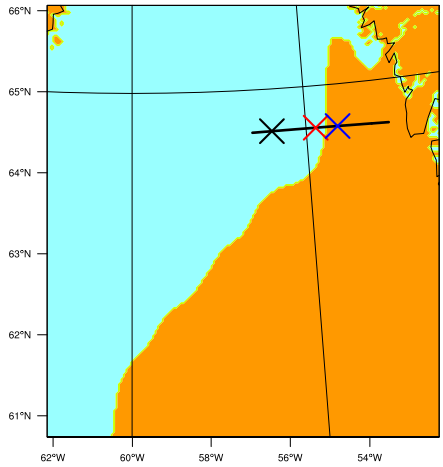

Figure 6.1: The black line is indicating the position of the cross section. The positions of the vertical profiles are marked with colored crosses. The light blue area represents the sea ice.

6.1 Cross section

The simulated section crossing the ice edge is illustrated in Figure 6.3. It also contains three vertical lines, which indicate the positions of wind and potential temperature profiles. Here, only the lowest 2000 m of the atmosphere are shown. A well defined wind maximum close to the ice edge is clearly visible. The margin of the sea ice is characterized by a strong horizontal temperature gradient at the surface which arises due to heat fluxes from the ocean. The height of the jet coincides with the capping

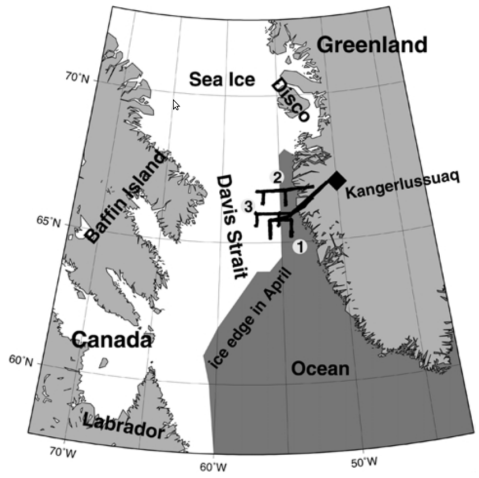

Figure 6.2: Shown are the three flights during the KABEG campaign crossing the ice edge. From DRÜE and HEINEMANN (2001)

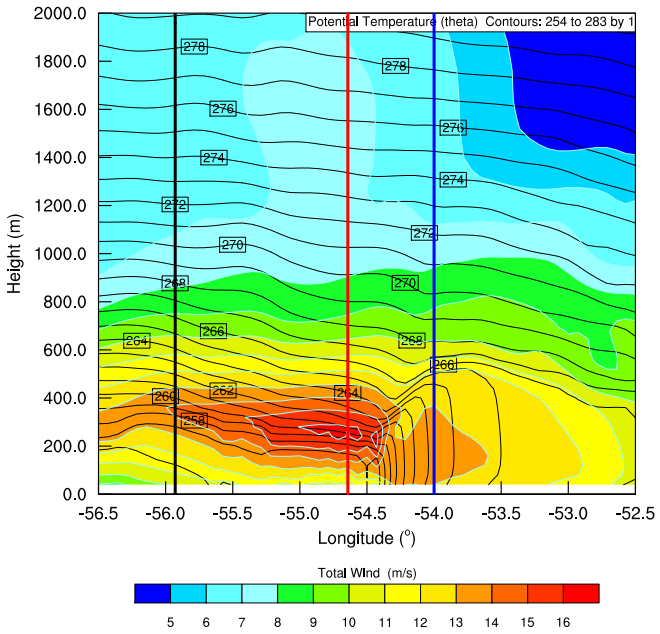

Figure 6.3: Cross section of total wind (colors) and potential temperature (contours). Vertical lines indicate the positions of profiles

inversion of the boundary layer. That configuration looks similar to Figure 5.6 which is a cross section for the case in 1993. This suggests that such low level jets at the sea ice edge seem to be a rather common feature at least in the WRF model. This case

from 1997 has the advantage that the results by DRÜE and HEINEMANN (2001) are based on measurements which allows us to validate the model results.

6.2 Wind and Potential Temperature Profiles

As mentioned above, the vertical lines in Figure 6.3 indicate the positions of profiles of potential temperature and total wind speed. Figure 6.4 shows the vertical distribution of potential temperature and Figure 6.5 displays the change of the wind profile. The profiles of the potential temperature can be clearly assigned to their positions in the cross sections. The two profiles over the sea ice (black and red line) have clearly lower temperatures at the surface in comparison to the profile over the open ocean. The potential temperature above the sea ice is at around 256K and above the ocean surface around 265K. Another difference can be seen in the boundary layer height. It is lowest close to the ice edge on the sea ice side (red line) at around 200 m and increases west and eastward. West of the ice edge the boundary layer height increases to around 300 m. A tremendous increase can be seen when crossing the ice edge and continuing further east over open ocean. As the green line in Figure 6.4 shows, the boundary layer height is around 600 m over the open ocean, this is a triplication of the value close to the ice edge. Of course, this is a result of the large heat input from the ocean to the atmosphere. The open ocean profile reveals a very well mixed boundary layer, as there is almost no change in potential temperature within the lowest 450 m. The profiles over the sea ice are also near neutral, but with a tendency to a slightly stable boundary layer. A common feature of all three profiles is that they converge at around 600 m, this means that they become independent from the surface properties.

A similar profile was made for the total wind speed (Equation 4.1). Figure 6.5 shows the change of the total wind speed with height. The low level jet, already seen in Figure 6.3, is clearly visible (red line). The total wind speed reaches a maximum of around

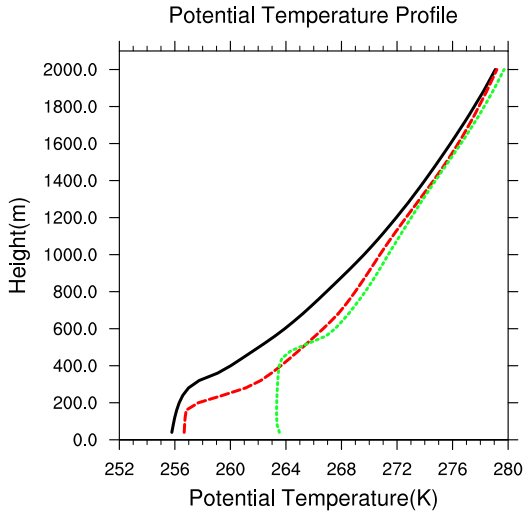

Figure 6.4: Vertical potential temperature profile

16 m/s at 260 m. The black line, which represents a profile 50km ice inward, displays a pronounced maximum as well. Here, the total wind speed reaches values up to 14.5 m/s and the height of the jet is elevated to 340 m. In the open ocean profile (green line), the wind speeds are quite uniform within the boundary layer. The wind is varying little between 12.5 m/s and 13.0 m/s. This corresponds to the potential temperature profile which shows a well mixed boundary layer. Similar to the potential temperature profiles is the fact that the graphs converge at a certain height, which in this case is at 500 m. A detailed analysis of the single wind components is not shown, but we know from DRÜE and HEINEMANN (2001) (Figure 3) that the wind was from northerly directions. Thus the wind is largely ice edge parallel.

As mentioned before, the advantage of the simulation of this event in 1997 is that there were measurements taken across the ice edge. Figure 6.6 displays the results of measurements by DRÜE and HEINEMANN (2001). The profiles are based on dropsonde measurements. Figure 6.6 shows profiles of the wind direction, wind speed, potential temperature and specific humidity. There is one profile over the ocean at a distance of 10km from the ice edge, one over the sea ice at 15km away from the

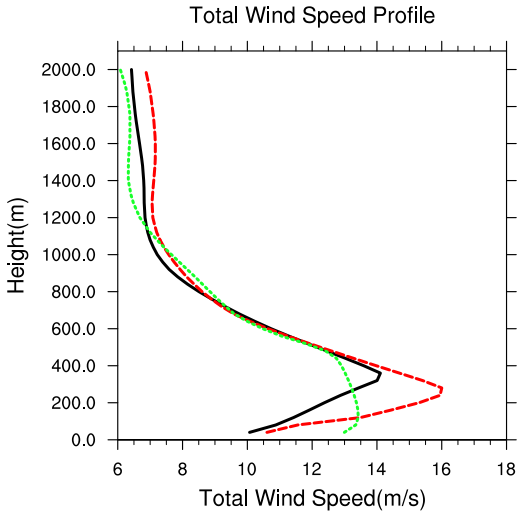

Figure 6.5: Vertical profile of the total wind speed

ice edge and another profile over the sea ice at 60km ice inward, respectively for each parameter. Thus, the positions of the measured profiles correspond to the positions of the simulated profiles.

The profiles close to the ice edge are similar. Both differ from the profile at 60km distance from the ice edge. Away from the ice edge the wind speed is about 6 to 7 m/s and close to the ice-ocean margin the wind speeds are ranging from around 11 to 14 m/s below 500 m. At 700 m all three profiles become more similar, indicating that the influence from the surface is not noticeable any longer. In the simulations this is evident a little bit lower at around 500 m. Above this threshold, the wind speeds of the measurement and the simulation are comparable. There, the wind speeds are between 6 m/s in the ocean profile and 6 to 8 m/s in the sea ice profiles. The main difference between the measurements and the simulation, however, is that there is no distinct low level wind speed maximum in the measurements. The highest wind speeds are found over the ocean and close to the ground. This fact questions the results of the WRF simulations. While the simulation of the 1993 and 1997 case revealed a good agreement, the measurements do not confirm the existence of a relative wind maximum at the ice

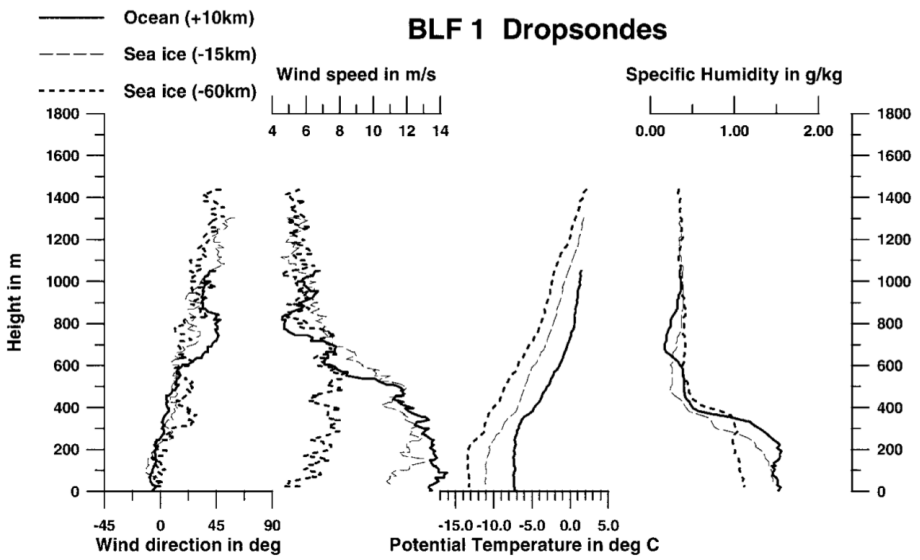

Figure 6.6: Aircraft measurements across the ice edge. Shown are dropsonde profiles over Ocean(fat full lines), over sea ice close to the edge(thin dashed lines) and ice inward (fat dashed lines). From DRÜE and HEINEMANN (2001)

edge just above the boundary layer.

There is more agreement between measurements and simulation regarding the potential temperature. In both cases the potential temperature is rising as the profiles get closer to the edge and highest over the open ocean, also the boundary layer height is highest over the open ocean. The close to neutral stratification within the boundary layer is another common feature. Differences are visible in the exact boundary layer height and the absolute temperatures. Over the open ocean the boundary layer height is lower in the measurements than in the simulation, the opposite is valid for the sea ice profiles. The potential temperature close to the edge in the simulation is different to the equivalent profile in the observations. The model has $-17°C$ where there were only $-11°C$ measured. Also, the potential temperature difference across the ice edge is different. The simulation shows about 7 K, whereas the difference in the measurement is only 4 K. This fact causes most likely that there is no distinct wind maximum in the measurements. The reduced potential temperature gradient causes a smaller thermal

wind and therefore, the actual wind is not decreased across the ice edge. The strong potential temperature gradient is also associated with a rapid increase of the boundary layer across the ice edge is. In the simulations, the boundary layer grows from around 200 m to 500 m. The measurements, however, do not show this rapid increase of the boundary layer height. Therefore, we do not expect a relative wind maximum which is associated with the rapid boundary layer height increase. The discrepancies in surface temperature differences are most likely caused by different surface sensible heat fluxes.

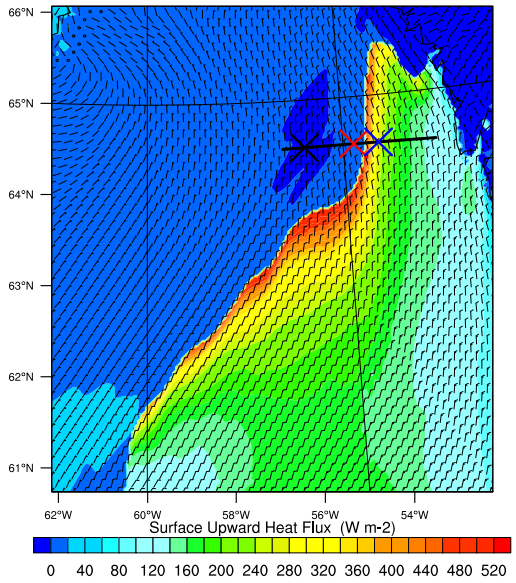

Figure 6.7: Upward Sensible Heat Flux

6.3 Surface Sensible Heat Fluxes

Recalling the extreme values of surface sensible heat flux for the 1993 case (Figure 5.24), a similar plot was made here. Figure 6.7 shows the upward sensible heat flux at the surface. The values close to the ice edge are still quite high, but not as extreme as for the 1993 case. The maximum upward heat flux at the ice edge is about $500\mathrm{W/m^2}$. This results from a smaller difference in skin surface temperature across the ice edge in

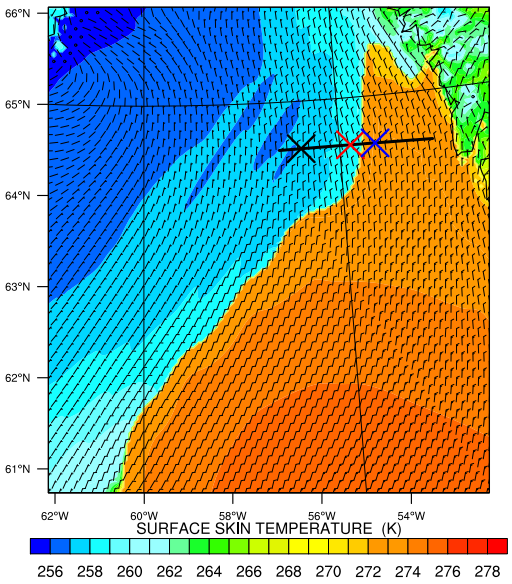

Figure 6.8: Skin Surface Temperature

comparison to the 1993 case. There the difference was 25K. The temperature of the sea ice skin surface in this case is circa 260K and the skin temperature of the ocean close to the ice edge is around 274K (Figure 6.8), which is a difference of 14K. Furthermore, the wind speed is important for surface heat fluxes. The 10 m wind speed shown in Figure 6.8 is lower than in the 1993 case (Figure 5.9). This contributes also to lower surface heat fluxes.

However, in comparison to the measurements by DRÜE and HEINEMANN (2001), the surface heat fluxes are still very large. They measured the sensible heat flux at 45 m (Figure 6.9). The largest values are found just at the sea side of the ice edge, there the maximum sensible heat flux is about $50\mathrm{W/m^2}$. At 45 m over the sea ice, the sensible heat flux is about $20\mathrm{W/m^2}$. It decreases towards the ice edge and reaches a minimum of about $10\mathrm{W/m^2}$ at approximately 10 km away from the ice edge. The 20km range from -10km to 10km relative distance to the ice edge reveals an increase of the turbulent sensible heat flux from $10\mathrm{W/m^2}$ to $50\mathrm{W/m^2}$. Assuming that the measurements at 45 m are within the surface layer the flux measurements at 45 m are comparable with surface

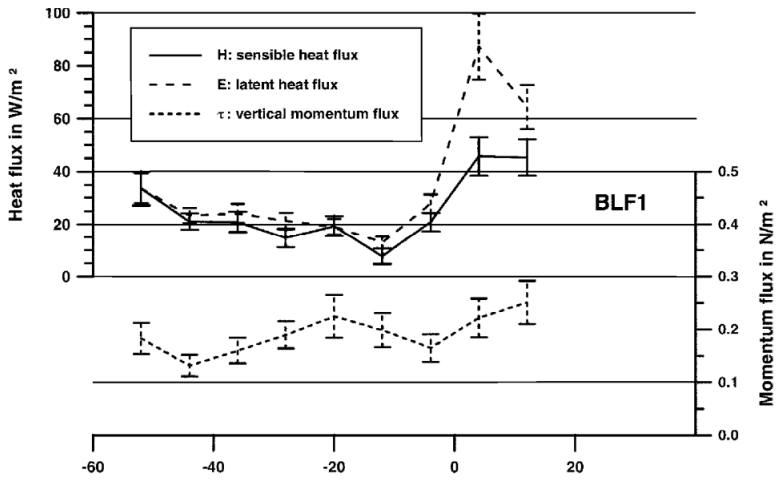

Figure 6.9: Turbulent fluxes at 45 m height. Figure 15a in DRÜE and HEINEMANN (2001)

fluxes. The WRF simulation, however, showed surface fluxes which are about 10 times the value of the 45 m measurement. A thorough study about the representation of surface heat fluxes in the WRF model could be a starting point for another investigation.

The comparison between measurements and model simulation highlighted a discrepancy in the total wind speed over sea ice. The model overestimates the wind speed and has a low level jet close to the ice edge which cannot be found in the measurements. This is probably due to the very large surface heat fluxes, that supply too much energy to the atmosphere. However, as we already saw in the 1993 case, large surface sensible heat fluxes are not directly forcing the low level jet, but rather slow down the flow in the proximity. A detailed analysis as in chapter 5 is presented in the following sections.

6.4 Geostrophy in the 1997 Case

The 1997 case was also tested in terms of geostrophy. Here, the edge-along wind is close to the meridional wind component since the sea ice edge is rather south-north

aligned. The geostrophic wind and the actual wind are plotted in Figure 6.10. Both winds are not as consistent as in the 1993 case, which might be due to the the presence of Greenland's topography that is interfering with the northerly flow. However, the actual edge-along wind and the geostrophic wind are comparable. This is valid especially above the boundary layer. There is also high pressure over the sea ice and low pressure over the open ocean (Figure 6.11). This leads to a northerly geostrophic wind which is directed against the thermal wind. This setup is similar to the 1993 case.

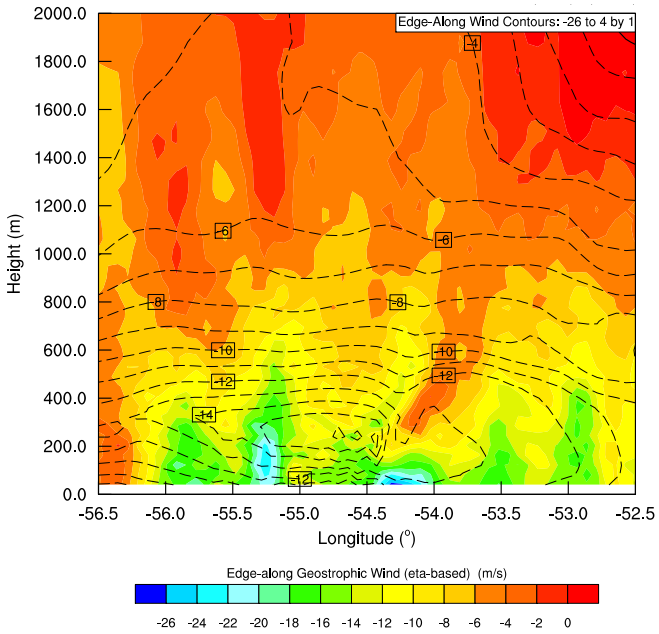

Figure 6.10: East-west cross section at 64.5 °N showing the actual wind along the ice edge (contours) and the geostrophic wind along the ice edge (colors).

Within the boundary layer, the northerly geostrophic wind is increasing and has its minimum at the surface close to the ice edge. There it reaches values of up to $-26\,\mathrm{m/s}$. There is a secondary minimum within the boundary layer over the sea ice at 55.5°W which might be caused by irregularities in the sea ice. But as already seen in Figure 5.15, there is an interesting feature at the capping inversion close to the ice edge. There is a relative maximum just below the inversion. To the west of the inversion, a relative

minimum exists. The maximum follows the thermal wind relation as it is described in the 1993 case. The relative minimum just to the west of the inversion could possibly caused by a small dip in the isentropes (see Figure 6.12).

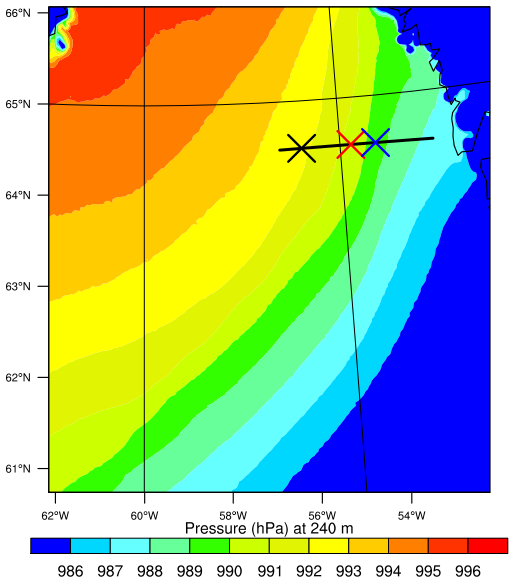

Figure 6.11: Horizontal plot showing the pressure at 240 m, which corresponds to the low level jet height. The black line indicates the location of the east-west cross section.

The ageostrophic wind together with the potential temperature is shown in Figure 6.12. It stands out that the characteristics of the ageostrophic wind is very similar to the 1993 case. The values above the boundary layer vary between -6 and 2 m/s. Within the boundary layer, the same dipole pattern is visible as it is in Figure 5.16, even if the absolute values are somewhat smaller. This is also true regarding the boundary layer height which is lower than in the 1993 case. Close to the surface at the ice edge there is a maximum, which implies a northward ageostrophic wind component. So the actual wind is slowed down in comparison to the geostrophic wind due to frictional processes. The opposite happens at the inversion layer, here the actual wind speed is higher in comparison to the geostrophic wind. Again, the reason is the inertia of the actual flow. However, there is again no distinctive low level jet in the ageostrophic

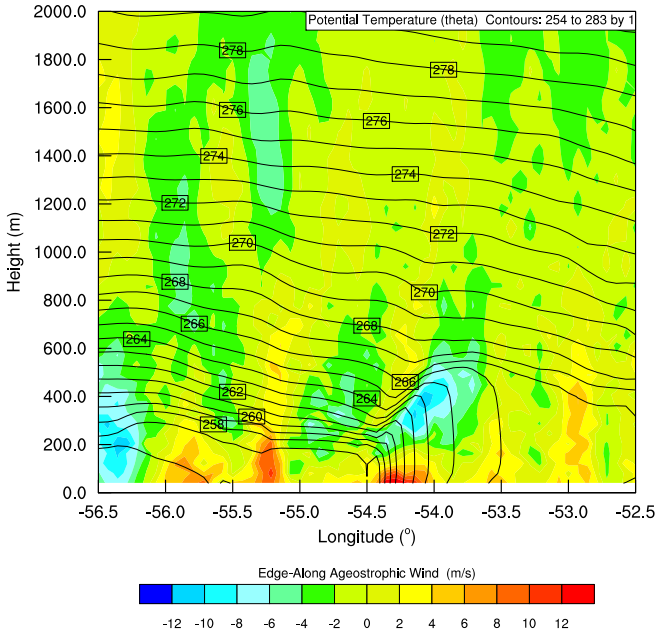

Figure 6.12: East-west cross section at 64.5 °N showing the ageostrophic wind along the ice edge (colors) and the potential temperature (contours).

component. Thus the low level jet close to the ice edge (Figure 6.10) does not deviate much from geostrophy.

The thermal wind is depicted in Figure 6.13 and is similar to the thermal wind shown in Figure 5.23. The absolute values are about half of the values observed in the 1993 case which is due to the less strong potential temperature gradient across the ice edge. However, the geostrophic wind increases with height, which means that the northerly geostrophic wind is slowing down to almost 0 m/s. The sloping inversion forms a potential temperature gradient which is reversed to the gradient at the surface and therefore, the geostrophic wind is again decreasing across this inversion to circa -12 m/s.

Thus, the explanation for the appearance of the low level jet in the 1993 case might also be applied here, although it is less obvious. Summarizing this section, it can be said that the WRF simulations of the atmosphere in the vicinity of the sea ice edge

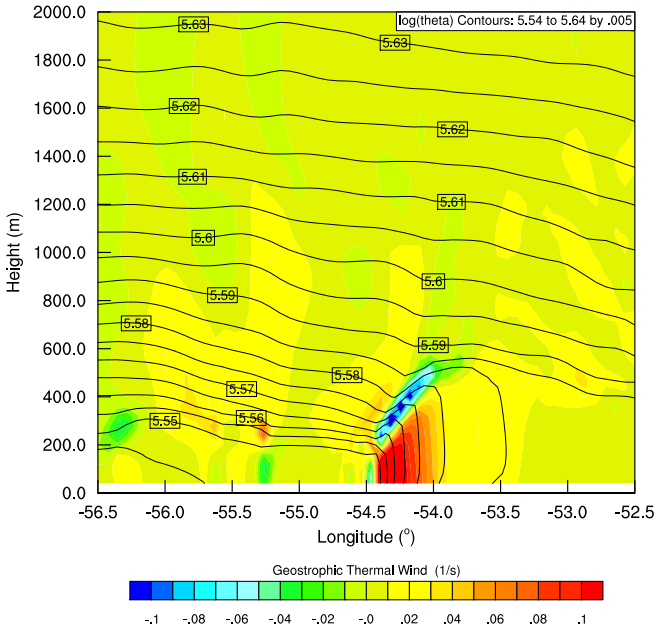

Figure 6.13: East-west cross section at 64.5 °N showing the actual wind along the ice edge (contours) and the geostrophic wind along the ice edge (colors).

are consistent. The case in 1993 as well as the case in 1997 exhibited a wind maximum just above the boundary layer and with a strong temperature gradient on the southern (1993 case) or eastern (1997 case) side. It was hypothesized that the pronounced low level jet is not directly an outcome from the strong baroclinicity at the margin between sea ice and open ocean but rather exists due to the slowing down of the surrounding air masses, which is indeed caused by the strong frontal zone at the ice edge.

6.5 PolarWRF Simulations of the 1997 Case

The previous section showed that the WRF simulation of the 1993 and 1997 case agree well in terms of geostrophy. However, section 6.2 revealed a discrepancy between the WRF simulation and a measurements taken by an aircraft within the boundary layer. Therefore, the modified WRF version PolarWRF was used as well. The results of the PolarWRF simulation are shown in Figure 6.14. There is a local wind maximum visible,

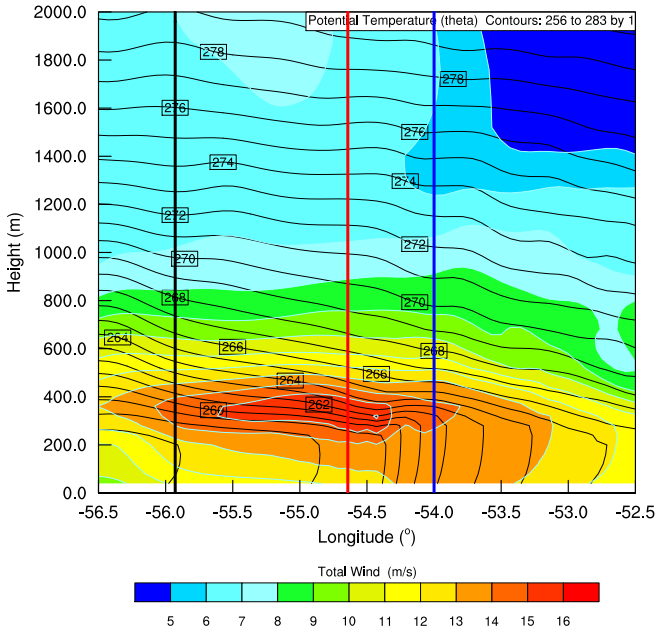

Figure 6.14: East-west cross section at 64.5°N of the PolarWRF simulation. Colors illustrating the total wind and contours showing the potential temperature

which is of comparable strength as in the regular WRF simulation. In comparison to Figure 6.3, the horizontal extension of the low level jet is larger, the jet even crosses the ice edge at around 54.5°W. This is a direct result from the modified boundary layer. The temperature gradients are much smaller than in the regular WRF simulation. This is true for the boundary layer front at the ice edge as well as for the inversion layer separating the boundary layer from the free atmosphere. Especially, the sloped inversion layer east of the low level jet in Figure 6.3 is not present anymore. An explanation of the decreased temperature difference can be given when remembering that PolarWRF has an improved surface energy balance. Figure 6.15 shows the upward surface sensible heat flux. Just on the sea side of the ice edge are the maximum sensible heat fluxes about 250W/m^2. This is just half of the heat flux found in the regular WRF simulation (Figure 6.7). Thus, the heat input from the ocean to the atmosphere is much smaller and consequential are the temperature differences much smaller, which in turn leads to a reduced thermal wind.

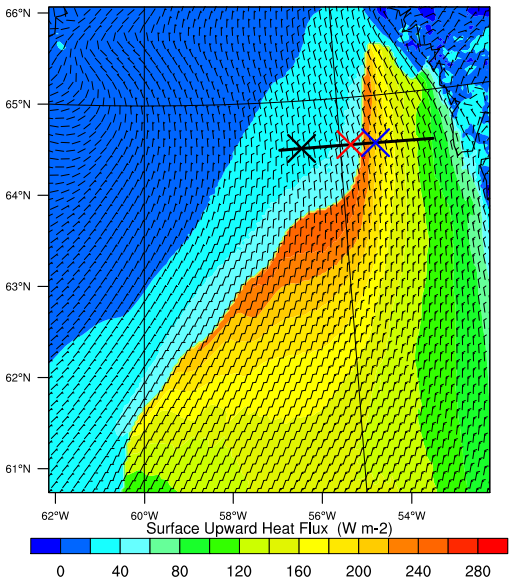

Figure 6.15: Upward surface sensible heat flux from the PolarWRF simulation.

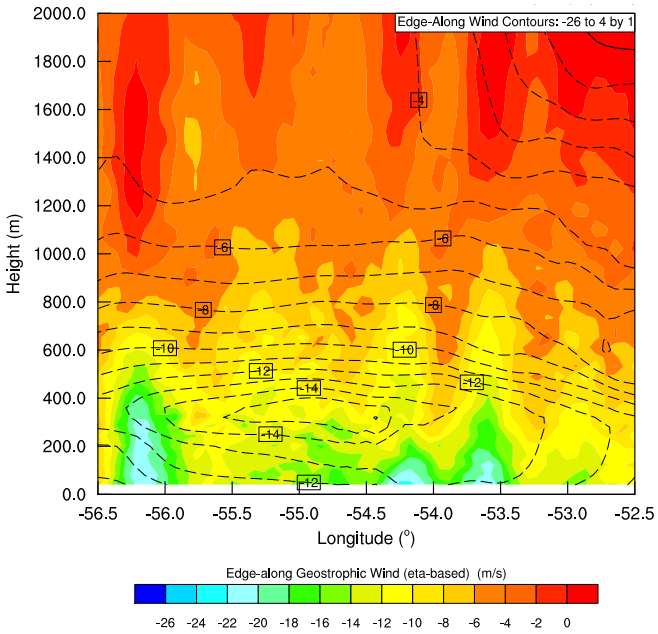

Figure 6.16: East-west cross section of the PolarWRF simulation. Illustrated is the geostrophic wind along the ice edge (colors) and the actual wind along the ice edge (contours).

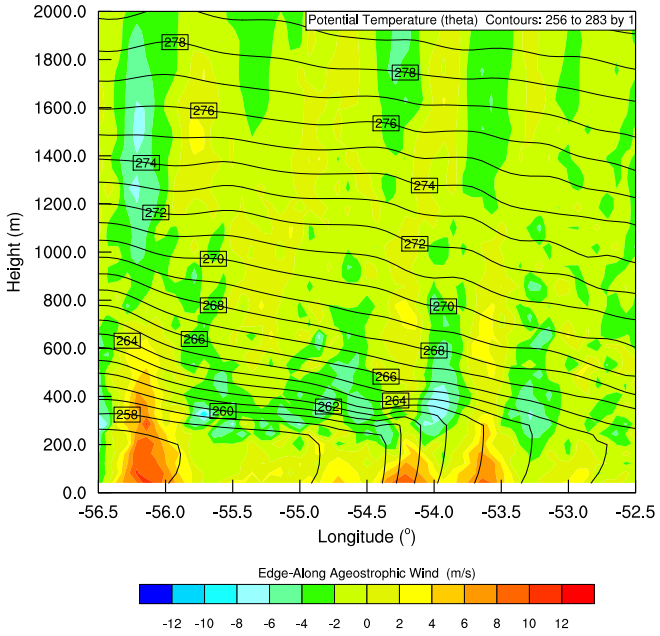

Figure 6.17: East-west cross section at 64.5°N of the PolarWRF simulation. Colors illustrating the ageostrophic wind along the ice edge and contours showing the potential temperature.

6.5.1 Geostrophy in PolarWRF simulation

The previous section showed that the low level jet is extending over the ocean, due to reduced surface sensible heat flux. The potential temperature gradient is reduced a lot. Hence, the geostrophic wind is not expected to significant slow down at the ice edge. Figure 6.16 confirms this assumption. The distinct dipole pattern at the ice edge, existent in the large heat flux case is not observable here. The geostrophic wind is more uniform across the ice edge as the influence of the ice edge is in general reduced. The surface minimum of the geostrophic wind at the ice edge was exceeding $-26\,\mathrm{m/s}$ before and is now decreased to $-22\,\mathrm{m/s}$. Figure 6.17 certifies the reduced influence of the ice edge. There is still a maximum at the surface and a minimum at inversion height but it is less pronounced. In particular, the minimum at inversion height is much weaker due to the lacking of the front at the surface. The precedent argumentation suggest that when there is no surface heat flux at all, there should be no distinct low level jet

but rather an extended band of strong wind due to the large scale pressure gradient. A WRF run without surface fluxes is presented in section 6.6.

6.5.2 1997 PolarWRF Profiles

In section 6.2, a deviation of the WRF smulations from measurements was detected. The aircraft based measurements did not content a low level jet. In addition, the wind speed over the sea ice within the boundary layer was overestimated by the model. The same profiles as in Figure 6.4 and Figure 6.5 were produced for the PolarWRF output (Figures 6.18, 6.19). The difference between surface wind speed and maximum wind speed became smaller in the profiles over the sea ice, which makes the wind maximum less pronounced. The maximum wind speed, however, is still about 16 m/s. The largest wind speed found in the profile over the open ocean increased to about 14 m/s. Thus, the ocean profile became more similar to the measured profile. Thus, the PolarWRF model exhibit an improvement regarding the boundary layer over the open ocean close to the sea ice edge. This was expected since the reduced surface sensible heat flux creates weaker potential temperature gradients and therefore, the thermal wind decreases. Thus, the actual wind at the wind maximum height is less decreased. In comparison to the measurements however, the profiles over the sea ice are still not well simulated. In comparison to the measurement, the profiles over the sea ice are still not well simulated. The profile close to the edge still shows a distinctive wind maximum, which is not existent in the measurement. The solid black line in Figure 6.18 illustrates the profile at 60 km distance from the ice edge. There is a large discrepancy between simulation and measurements. The simulated profile shows a wind maximum of about 14.5 m/s. The measured profile 60km ice inward in DRÜE and HEINEMANN (2001), however, has winds around 7 m/s within the boundary layer and slightly lower values above. We hypothesize that the friction over sea ice is not accurately modeled in WRF and also PolarWRF. For example, rafting and ridging is a process which is not included in WRF and PolarWRF but which can crucially change the surface roughness.

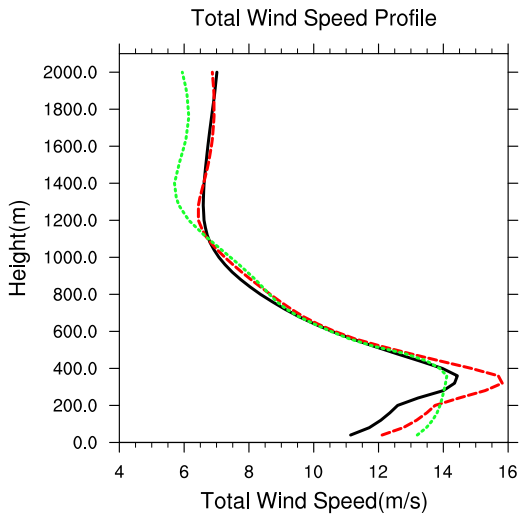

Figure 6.18: PolarWRF profiles of total wind speed. Line colors are according to the position in the cross section (Figure 6.14).

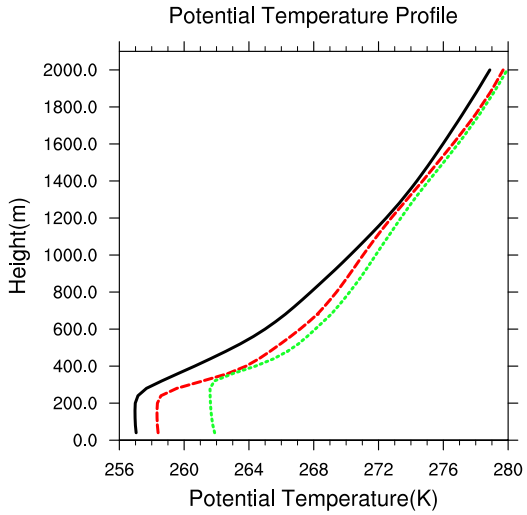

Figure 6.19: PolarWRF profiles of potential temperature. Line colors are according to the position in the cross section (Figure 6.14).

6.6 Simulation of the 1997 Case without Surface Fluxes

The 1997 case was also simulated with turned off surface fluxes. Section 5.8 already showed that a WRF run without surface fluxes does not produce low level jets at the ice edge. Figure 6.20 illustrates this finding for this case. The wind speed at the position of the original wind maximum is even higher than in the control run. In fact, the wind speed increases toward the east and reaches a maximum between 54°W and 53.5°W over the ocean. The 1993 case also showed that there is no thermal wind slowing down the actual wind when the surface fluxes are turned off. The same statement can be made here. There is a wind maximum appearing over the ocean which cannot be related to the ice edge. As in the 1993 case, an analysis of this low level jet is not part of this thesis.

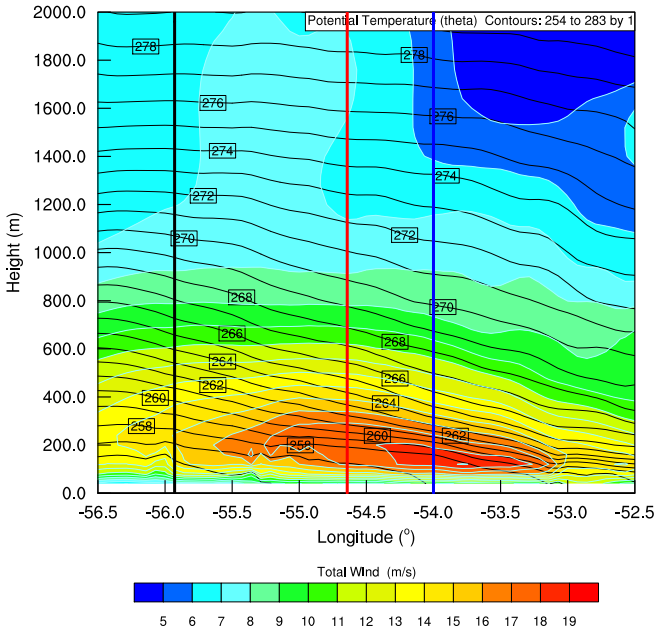

Figure 6.20: East-west section at 64.5°N of the WRF run without surface fluxes. Shown is the total wind (colors) and the potential temperature (contours).

The difference between the control run and the noflux run is shown in Figure 6.21. The isentropes in Figure 6.21 are from the control run for a better orientation. The values are mostly varying around 0 m/s. However, there is a distinct minimum within the boundary layer. This means that the total wind speed is larger in the noflux simulation than in the control run. So it is clear that the total wind in the original simulation is slowed down. However, the difference in wind speed at the low level jet position is between 0 and -2 m/s. This confirms the result from section 5.8, that the maximum wind speed in Figure 6.20 is not forced by the ice edge. The wind speed would be even higher without the large surface fluxes near the ice edge.

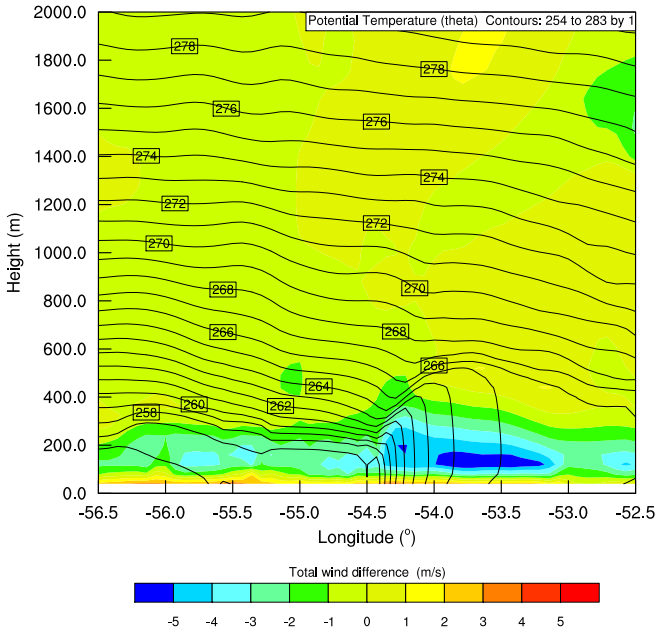

Figure 6.21: East-west cross section at 64.5 °N showing the actual wind along the ice edge (contours) and the geostrophic wind along the ice edge (colors).

The analysis of the 1997 case confirms the findings in the 1993 case. The low level jet seen in Figure 6.3 is not directly caused by the ice edge as in terms of forcing. Too high surface fluxes led to too strong fronts at the ice edge and slowed down the wind within the boundary layer. A simulation made with the modified WRF version called Polar-

WRF revealed more realistic surface fluxes and the wind and potential temperature profiles were in better agreement with those presented in DRÜE and HEINEMANN (2001). Finally, a simulation without surface fluxes was shown, although not realistic, the argument was confirmed that the low level jet is not directly due to the ice edge.

Chapter 7

Summary and Outlook

We presented low level jets at the edge between sea ice and open ocean. Three papers were the basis for this study which were all simulated with the WRF model. First, there was a study by SHAPIRO and FEDOR (1989). They described measurements from a flight campaign in 1984. However, simulations with WRF could not reproduce this strong wind maximum. Uncertainties in the location of the sea ice edge, as well as the proximity to Svalbard were indicated at possible reasons. As this is the only measured ice edge jet, a simulation which reproduces these measurements would improve the understanding of the formation of wind maxima at the ice edge a lot. This thesis excluded the 1984 case from further analysis due to the aforementioned reasons.
The paper by GRØNÅS and SKEIE (1999) also contained a low level jet at the ice edge. However, their results of the ice edge jet are only based on simulations of the NORLAM model. A detailed explanation was not given. However, the results by GRØNÅS and SKEIE (1999) could be well reproduced with the WRF model. The paper did also contain an analysis of geostrophy, thus, this was done for the WRF model results as well. This analysis revealed the greatest inside in the processes at the ice edge. The major finding was that the low level jet, as described by GRØNÅS and SKEIE (1999) is in fact in geostrophic balance. South of the low level jet, the geostrophic wind slows down rapidly to 0m/s. This is a direct outcome of the strong potential temperature gradient

across the ice edge and can be explained by the thermal wind relation. Extreme values in upward surface sensible heat flux of about 2000W/m^2 were observed and caused this strong potential temperature gradient. The actual wind is then adapting to the changed geostrophic relations. Also, the wind slows down below the boundary layer, due to frictional processes. The wind is naturally decaying upwards, because of tilted isentropes which cause a thermal wind. These reasons make the low level jet look like a local wind maximum forced by the ice edge, but it is not. Thus the ice edge jet might not be considered as a low level jet in the common sense. Further experiments confirmed this argument. A modified version of WRF called PolarWRF was used. This version, designed for polar environments, has an improved surface energy balance, as well as variable sea ice and snow thickness. The main outcome, however, is a reduced surface sensible heat flux, which was about half of the flux obtained in the original run. This led to a weaker front at the ice edge and consequently to a reduced thermal wind. Hence, the actual wind was less slowed down and the wind maximum was not restricted to the ice edge anymore. The final proof of our argument was to run WRF without any surface fluxes. Of course, the strong front at the ice edge was then not existent any longer and therefore, the wind did not slow down close to the ice edge. At the former location of the low level jet, the same wind speed values were still reached, but this was not the maximum wind speed any longer. The wind increased toward the south and reached a maximum far away from the ice edge.

The last paper in this study was DRÜE and HEINEMANN (2001). They also write about measurements taken by an aircraft. The atmospheric situation is comparable to GRØNÅS and SKEIE (1999), which means high pressure over the ice and low pressure over the ocean, which leads to a wind almost parallel to the ice edge. Therefore we would expect comparable results like in the 1993 case. The WRF simulations indeed showed a similar behavior. There was a low level wind maximum close to the ice edge. This speaks for the consistency of the model. However, there was no low level jet in the measurements. Again, very large surface heat fluxes appeared and causing strong

potential temperature gradients across the ice edge. Hence, a similar mechanism like in the 1993 case developed. The PolarWRF simulations with more moderate surface fluxes yielded results closer to the measurements. Here, another issue turned up, i.e., the parameterizations of the friction over sea ice is probably not very accurate. This is another starting point for further studies regarding the modeling of the boundary layer over sea ice. The model run without surface fluxes showed similar results to the 1993 case. The wind was increasing towards the open ocean. Here, the wind speed at the low level jet location was even higher than in the original WRF simulation. This means that the ice edge in this case even slows down the low level jet.

In the future, a thoroughly study of idealized cases of flow at the ice edge will be conducted. The aim will be to understand the atmospheric dynamics at the ice edge also with flow from different directions. For example, the thermal wind in the 1993 and 1997 case was directed against the large scale wind. Thus, the forcing due to the ice edge resulted in minimum wind speeds. In the 1984 case, however, the large scale wind was aligned with the thermal wind. Thus, the ice edge most likely caused the wind maximum. The sensitivity to different angles of the wind relative to the ice edge will be tested. It is also possible to test the sensitivity to the surface sensible heat flux. Also different boundary and surface layer parameterizations can be part of an analysis. Of course, the results of the numerical simulations have to be validated by measurements. So it is necessary to obtain more data from measurements at the MIZ.

Bibliography

BJERKNES J. 1919. On the structure of moving cyclones. *Monthly Weather Review* **47**: 95.

BJERKNES J and SOLBERG H. 1922. Life cycles of cyclones and the polar front theory of atmospheric circulation. *Geofys. Publ.* **3**(1).

BJERKNES V. 1921. *On the dynamics of the circular vortex: with applications to the atmosphere and atmospheric vortex and wave motions*. Geofysiske publikationer, I kommission hos Cammermeyers bokhandel.

BLUESTEIN H. 1993. *Synoptic-dynamic meteorology in midlatitudes: Volume ii: Observations and theory of weather systems*. Synoptic-dynamic Meteorology in Midlatitudes: Observations and Theory of Weather Systems, Oxford University Press, USA, ISBN 9780195062687.

DRÜE C, HEINEMANN G. 2001. Airborne investigation of arctic boundary-layer fronts over the marginal ice zone of the davis strait. *Boundary-layer meteorology* **101**(2): 261–292.

ELIASSEN A. 1951. Slow Thermally or Frictionally Controlled Meridional Circulation in a Circular Vortex. *Astrophysica Norvegica* **5**: 19.

ELIASSEN A. 1962. On the Vertical Circulation in Frontal Zones. *Geofysiske publikationer* **24**: 147–160.

GLENDENING JW. 1994. Dependence of boundary layer structure near an ice-edge coastal front upon geostrophic wind direction,. *Journal of Geophysical Research* **99**(D03): 5569–5581.

GRØNÅS S, SKEIE P. 1999. A case study of strong winds at an arctic front. *Tellus A* **51**(5): 865–879.

HOLTON J. 2004. *An introduction to dynamic meteorology*. The International Geophysics Series, Vol 88, Elsevier Academic Press, ISBN 9780123540157.

HOSKINS BJ. 1975. The geostrophic momentum approximation and the semi-geostrophic equations. *J. Atmos. Sci.* **32**(2): 233–242.

LANGLAND RH, TAG PM, FETT RW. 1989. An ice breeze mechanism for boundary-layer jets. *Boundary-Layer Meteorology* **48**: 177–195. 10.1007/BF00121789.

LIN Y. 2010. *Mesoscale dynamics*. Cambridge Atmospheric and Space Science Series, Cambridge University Press, ISBN 9780521004848.

MILLER J. 1948. On the Concept of Frontogenesis. *Journal of Atmospheric Sciences* **5**: 169–171.

NAMIAS J, CLAPP PF. 1949. Confluence theory of the high tropospheric jet stream. *J. Meteor.* **6**(5): 330–336.

ØKLAND H. 1998. Modification of frontal circulations by surface heat flux. *Tellus A* **50**(2): 211–218.

PETERSEN GN, RENFREW IA. 2009. Aircraft-based observations of air–sea fluxes over denmark strait and the irminger sea during high wind speed conditions. *Quarterly Journal of the Royal Meteorological Society* **135**(645): 2030–2045, doi: 10.1002/qj.355, URL `http://dx.doi.org/10.1002/qj.355`.

PETTERSSEN S. 1936. *Contribution to the theory of frontogenesis*, *Geofysiske publikationer*, vol. 6.

PRESS WH, FLANNERY BP, TEUKOLSKY SA, VETTERLING WT. 1992. *Numerical Recipes in Fortran: The Art of Scientific Computing*. Cambridge University Press, 2 edn, ISBN 052143064X.

SAWYER J. 1956. The Vertical Circulation at Meteorological Fronts and its Relation to Frontogenesis. *PROCEEDINGS OF THE ROYAL SOCIETY OF LONDON SERIES A-MATHEMATICAL AND PHYSICAL SCIENCES* **234**(1198): 346–362.

SHAPIRO MA, FEDOR LS. 1989. A case study of an ice-edge boundary layer front and polar low development over the norwegian and barents sea. In: *Polar and Arctic Lows*. Twitchell, P.F. Rasmussen, E.A. abd Davidson,K.L.(eds.). A.Deepak Publishing, pp. 257–277.

SKAMAROCK W, KLEMP J, DUDHIA J, GILL D, BARKER D, DUDA M, yu HUANG X, WANG W. 2008. A description of the advanced research wrf version 3. Technical report.

STULL R. 1988. *Intro to boundary layer*. Atmospheric Sciences Library, Kluwer Academic Pub, ISBN 9789027727695.

VIHMA T, JOHANSSON MM, LAUNIAINEN J. 2009. Radiative and turbulent surface heat fluxes over sea ice in the western weddell sea in early summer. *Journal of Geophysical Research: Oceans (1978–2012)* **114**(C4).

WALLACE J, HOBBS P. 2006. *Atmospheric science: An introductory survey*. International Geophysics, Elsevier Science, ISBN 9780080499536.